e-ISSN: 2687-6698 **Research Article**

Turkish Journal of

Analytical Chemistry

TurkJAC

https://dergipark.org.tr/tr/pub/turkjac

Model-based and molecular-level evaluation of methyl orange adsorption onto a hazelnut shell-based carbonaceous adsorbent

Nagihan Soyer[1]*, Sema Salgın[1], Uğur Salgın[1]

[1] Sivas Cumhuriyet University, Faculty of Engineering, Department of Chemical Engineering, 58140 Sivas, Türkiye

Abstract

Methyl orange adsorption onto a hazelnut shell-based carbonaceous adsorbent was investigated using an integrated experimental, statistical, physicochemical, and density functional theory approach. Under the investigated kinetic conditions (C_0 = 42.65 mg/L, pH 3.0, 30.4 °C, and 225 rpm), the adsorption capacity reached 32.183 ± 0.086 mg/g at 360 min. Nonlinear model comparison identified the pseudo-first-order model as the most suitable empirical description of the kinetic data, while Weber–Morris and Boyd analyses were consistent with contributions from both external mass transfer and intraparticle diffusion. Equilibrium data obtained at 10.0–40.0 °C were evaluated using Freundlich, Langmuir, and Redlich–Peterson models. Freundlich provided a robust description across the investigated temperatures, supporting heterogeneous adsorption behavior. Apparent thermodynamic analysis indicated favorable and endothermic adsorption tendencies. N_2 adsorption–desorption analysis showed that the BET surface area decreased from 812.4 to 515.8 m^2/g after methyl orange uptake, accompanied by substantial reductions in accessible pore volume and microporosity, consistent with partial pore occupation and restricted accessibility of narrower pores. FTIR, XRD, SEM/EDX, and surface-charge analyses provided complementary evidence for methyl orange uptake and favorable interactions under acidic conditions. Density functional theory calculations yielded a model-level adsorption energy of −179.8 kJ/mol and supported π-related interactions, dispersion forces, electrostatic complementarity, and localized hydrogen bonding. Overall, Methyl orange adsorption by hazelnut shell-based carbonaceous adsorbent was governed by surface heterogeneity, pore accessibility, coupled mass-transfer processes, and multiple non-covalent interactions.

Keywords: Methyl orange, adsorption, hazelnut shell, adsorption modeling, density functional theory

1. Introduction

Synthetic dyes are among the most problematic organic pollutants released into aquatic environments because of their high color intensity, chemical stability, and resistance to conventional biological degradation processes [1,2]. Among the various dye classes, azo dyes constitute the largest group used in textile, printing, paper, leather, cosmetic, and pharmaceutical industries [1,3]. The discharge of dye-containing effluents into natural waters can reduce light penetration, suppress photosynthetic activity, alter dissolved oxygen balance, and negatively affect aquatic ecosystems [1,2]. Consequently, the development of efficient and sustainable technologies for dye removal remains an important environmental challenge.

Methyl orange (MO) is a representative anionic azo dye that is widely employed as a model pollutant in adsorption studies because of its well-defined molecular structure, high aqueous solubility, and pH-dependent ionic behavior [4,5]. The molecule contains aromatic rings, an azo linkage (–N=N–), and a sulfonate group, which together provide multiple interaction sites for adsorption onto carbonaceous materials. These structural characteristics allow MO to interact with adsorbent surfaces through electrostatic attraction, π–π stacking, hydrogen bonding, and other non-covalent interactions depending on the solution chemistry and adsorbent surface properties [4–6]. Therefore, MO is frequently used not only as a target pollutant but also as a probe molecule for investigating adsorption mechanisms on porous carbon materials.

Among the available wastewater treatment technologies, adsorption is generally regarded as one of the most effective and practical approaches because of its operational simplicity, high removal efficiency,

Citation: N. Soyer, S. Salgın, U. Salgın, Model-based and molecular-level evaluation of methyl orange adsorption onto a hazelnut shell-based carbonaceous adsorbent, Turk J Anal Chem, 8(3), 2026, 190–218.

***Corresponding author:** nsoyer@cumhuriyet.edu.tr

Received: June 29, 2026
Accepted: September 01, 2026
https://doi.org/10.51435/turkjac.1980845

adaptability to dilute pollutant concentrations, and ease of implementation [2,7]. Activated carbon (AC) remains one of the most widely used adsorbents owing to its developed pore structure, high specific surface area, and strong affinity toward organic contaminants [7,8]. However, the relatively high production cost of commercial AC and growing sustainability concerns have stimulated interest in the conversion of agricultural residues into low-cost carbonaceous adsorbents [8]. In this regard, biochars and ACs produced from biomass resources have attracted considerable attention because they combine waste valorization with efficient pollutant removal performance.

Recent studies have shown that biomass-derived carbon materials can effectively remove MO from aqueous solutions when their pore architecture and surface chemistry are suitably developed. Chitosan-modified rice husk biochar exhibited enhanced adsorption performance compared with pristine biochar due to the introduction of amino and hydroxyl functional groups that increased surface affinity toward MO [9]. Iron-modified poultry-manure biochar showed significantly improved adsorption capacity as a result of additional iron-associated active sites and enhanced surface interactions [10]. Likewise, AC prepared from spent coffee grounds displayed strong affinity toward MO and exhibited adsorption behavior consistent with surface heterogeneity described by the Freundlich isotherm model [11]. Similar observations have been reported for N-doped activated carbons and ZnO-modified activated carbons, further highlighting the importance of surface chemistry in controlling adsorption performance [5,12]. Collectively, these studies indicate that MO uptake by biomass-derived carbonaceous materials is controlled not only by surface area and porosity but also by the type, density, and distribution of surface interaction sites, including oxygen-containing groups, heteroatom-related sites, and inorganic modification-derived active domains.

The adsorption of MO onto carbonaceous materials is generally governed by a combination of electrostatic interactions, π–π electron donor–acceptor interactions, hydrogen bonding, pore-filling effects, and diffusion-related transport phenomena [5,6,10]. Under acidic conditions, protonation of oxygen-containing surface groups may generate positively charged adsorption sites that favor electrostatic attraction with the negatively charged sulfonate group of MO. Simultaneously, aromatic domains present within carbonaceous adsorbents can interact with the aromatic rings of MO through π–π stacking interactions. Because these mechanisms may occur concurrently, adsorption is rarely controlled by a single process. Consequently, comprehensive adsorption studies typically require kinetic, equilibrium, diffusion, and thermodynamic analyses to evaluate adsorption behavior and rate-controlling features [6,12]. However, kinetic and isotherm models provide model-dependent descriptions of adsorption behavior and should not be used alone as definitive evidence for a specific adsorption mechanism. Therefore, complementary surface charge, spectroscopic, and molecular-level analyses are needed to support mechanistic interpretation.

Hazelnut shell is an abundant lignocellulosic agricultural residue that represents a promising precursor for the production of carbonaceous adsorbents. Its high carbon content, widespread availability, and low economic value make it an attractive candidate for waste valorization and sustainable adsorbent production [13]. In the present context, the prepared material is referred to as a hazelnut shell-based carbonaceous adsorbent (HSCA). Furthermore, carbonization and activation processes can generate porous structures, oxygen-containing surface groups, and graphitic domains capable of interacting effectively with aromatic organic pollutants. Despite the large number of studies investigating MO adsorption using various biochars and activated carbons, relatively few studies have combined process optimization, kinetic evaluation, diffusion analysis, equilibrium modeling, apparent thermodynamic interpretation, surface charge characterization, Fourier-transform infrared spectroscopic evidence, and molecular-level computational investigation within a single framework. Moreover, adsorption mechanisms are frequently inferred mainly from experimental model fitting, whereas direct molecular-level evidence supporting the proposed interactions is often limited. Consequently, a remaining need is to connect the macroscopic adsorption behavior of MO with experimentally determined textural and surface characteristics of biomass-derived carbonaceous adsorbents and molecular-level information on the interactions responsible for adsorption.

In our previous study, response surface methodology (RSM) and artificial neural network (ANN) modeling were successfully employed to optimize the adsorption of MO onto HSCA, yielding optimum operating conditions of C_0 = 42.65 mg/L, m/V = 1.29 g/L, T = 30.4 °C, and pH 3.0 [14]. Although pH was not the dominant factor compared with initial concentration and adsorbent loading in the optimization study, acidic conditions were favored during numerical optimization, possibly due to enhanced protonation of the carbonaceous surface and improved interaction with anionic MO species [14]. Thus, pH 3.0 was selected in the present work not as an arbitrary condition but as the

optimized acidic region requiring further mechanistic clarification.

Building upon this optimized acidic adsorption region, the present study aims to provide an integrated physicochemical and molecular-level evaluation MO adsorption onto HSCA. The adsorption behavior of MO onto HSCA was investigated through kinetic, diffusion, equilibrium, and apparent thermodynamic analyses to evaluate rate-controlling behavior, surface heterogeneity, and temperature-dependent adsorption characteristics. Surface-charge measurements were used to establish the electrostatic state of HSCA under the experimental adsorption conditions, while N_2 adsorption–desorption, Fourier-transform infrared (FTIR) spectroscopy, X-ray diffraction (XRD) and scanning electron microscopy/energy-dispersive X-ray spectroscopy (SEM/EDX) analyses were employed to characterize the textural, surface-chemical, structural, morphological, and elemental properties and changes associated with MO adsorption. In parallel, density functional theory (DFT) calculations using a finite oxygen-functionalized polyaromatic carbon cluster were performed to investigate possible molecular-level interactions between MO and representative aromatic/graphitic and oxygen-containing surface domains of HSCA. Adsorption energy, electronic structure, and non-covalent interaction (NCI) analyses were used to further characterize possible adsorbate–surface interactions. The scientific contribution of the present work lies in integrating these macroscopic adsorption, adsorbent-characterization, surface-charge, and molecular-level computational results within a common framework, thereby relating the observed adsorption behavior to pore accessibility, surface functionality, carbon structure, and specific MO–surface interactions rather than inferring the adsorption mechanism from kinetic and equilibrium model fitting alone. Accordingly, the present study extends our previous process-optimization work from the prediction of optimum operating conditions toward a complementary physicochemical and molecular-level interpretation of MO adsorption onto HSCA.

2. Materials and Methods

2.1. Materials

MO (dye content 85%) was purchased from Sigma-Aldrich Chemie GmbH (Taufkirchen, Germany) and used without further purification. Hydrochloric acid (HCl, 37% w/w) and sodium hydroxide (NaOH, ≥ 98%), used for pH adjustment, were supplied by Merck KGaA (Darmstadt, Germany). Deionized water with a resistivity of 18.2 MΩ·cm was produced using a Milli-Q® Gradient purification system (Millipore Co., Billerica, MA, USA) and used for preparing MO stock solutions, calibration standards, and working solutions.

2.2. Preparation of hazelnut shell-based carbonaceous adsorbent

Hazelnut shells of the Foşa cultivar (*Corylus avellana* L.; shell thickness, 1.2 ± 0.1 mm) were obtained from a local processing facility in Arsin (Trabzon, Türkiye). The shells were washed with deionized water, dried at 105.0 °C to constant mass, crushed, and sieved to 2–4 mm. Carbonization and steam activation were performed using a modified procedure based on the method reported by Klushin et al. (2017) [15]. Approximately 25 g of the prepared shells were placed in a quartz reaction vessel (Ø120 × 330 mm; 620 mL) of a rotary/oscillatory tube furnace (TSO1 11/400, Carbolite Gero Ltd., Hope, UK), heated to 480.0 °C at 5.0 °C/min under N_2 (100 mL/min), and held for 25 min. The resulting char was cooled under N_2 and gently sieved to remove loose fines without further grinding. For activation, 10 g of char was heated to 850.0 °C at 10.0 °C/min under N_2 (130 mL/min). At 850.0 °C, deionized water was fed to an external heated evaporator at 0.30 mL/min, and the generated steam was introduced into the reactor with the N_2 stream. Activation was conducted at 850.0 °C for 90 min, resulting in a burn-off of 32%. The product was subsequently cooled under N_2, carefully ground, and sieved. The 150–500 μm fraction was washed with deionized water until the washing liquor reached a stable pH of approximately 6.05, dried at 105.0 °C to constant mass, and stored in airtight containers until use. This fraction was designated as HSCA.

2.3. Batch adsorption procedure

Batch adsorption experiments were performed to evaluate the adsorption of MO onto HSCA. The experimental conditions were selected based on the previously optimized adsorption region reported for MO removal onto HSCA [14]. Accordingly, all adsorption experiments were carried out under acidic conditions at pH 3.0. In each experiment, 100 mL of MO solution was transferred into a 250 mL amber Erlenmeyer flask. The solution pH was adjusted to 3.0 using 0.1 M HCl or 0.1 M NaOH and measured with a PB-11 pH meter (Sartorius AG, Göttingen, Germany). After pH adjustment, HSCA was added to the solution at an adsorbent dosage of 1.29 g/L. Prior to the main kinetic experiments, the effect of agitation speed was evaluated at 125, 225, and 325 rpm under otherwise identical selected kinetic conditions. Based on the resulting time-dependent adsorption profiles, 225 rpm was selected as the working agitation speed. Thereafter,

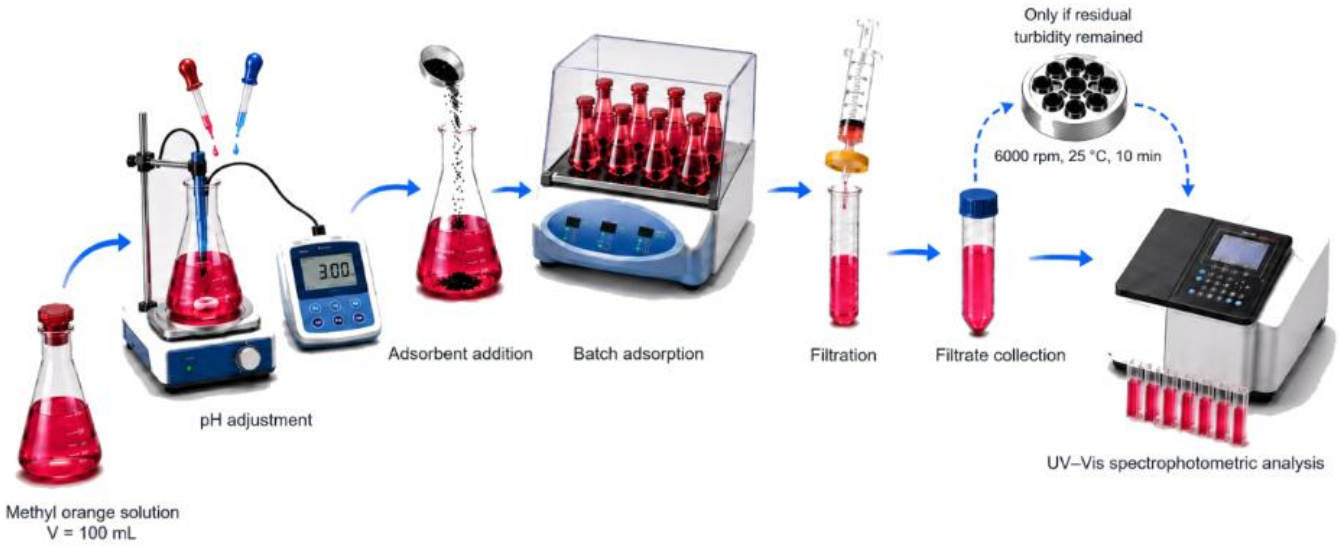


Figure 1. Schematic representation of the batch adsorption workflow used for MO removal onto HSCA.

all subsequent adsorption experiments were conducted at 225 rpm using a temperature-controlled orbital shaker (Barnstead International/LAB-Line MAXQ 4000, Melrose Park, IL, USA). The overall experimental workflow is schematically illustrated in Fig. 1. Independent flasks were used for all adsorption experiments. For the kinetic study, a separate flask was assigned to each predetermined contact time; thus, samples were not withdrawn sequentially from the same suspension. For equilibrium, isotherm, and thermodynamic experiments, the suspensions were shaken for the selected equilibrium contact time, while pH, adsorbent dosage, solution volume, and agitation speed were kept constant. The initial MO concentration and temperature were varied according to the corresponding equilibrium and thermodynamic experimental sets. All adsorption experiments were performed at least in triplicate, and the results were expressed as mean ± standard deviation (SD).

At the end of the specified contact time, each experimental sample was immediately passed through a 0.22 µm hydrophilic polyvinylidene fluoride (PVDF) membrane filter (Millex-GV, 33 mm; Merck Millipore Ltd., Carrigtwohill, Co. Cork, Ireland). Filtration was completed within approximately 1 min, and the first 15 mL of filtrate was discarded for membrane conditioning. Comparative measurements showed that filtration produced no relevant change in MO absorbance (absolute difference ≤ 0.003). When residual turbidity remained after filtration, the filtrate was additionally at 6000 rpm and 25.0 °C for 10 min. The residual MO concentration was determined using an ultraviolet-visible (UV-Vis) spectrophotometer (UV-1800, Shimadzu Corporation, Kyoto, Japan) at 504 nm. Since MO absorbance is affected by solution pH, concentration calculations were performed using a calibration curve prepared at pH 3.0.

The adsorption capacity at time t, q_t, was calculated using Eq. (1) [16,17]:

$$q_t = \frac{(C_0 - C_t)\,V}{m} \quad (1)$$

where q_t is the adsorption capacity at time t (mg/g), C_0 and C_t are the initial and time-dependent MO concentrations in the liquid phase (mg/L), V is the solution volume (L), and m is the adsorbent mass (g). For equilibrium adsorption experiments, C_t was replaced by C_e and q_t was expressed as q_e. The removal efficiency, Y%, was calculated using Eq. (2) [16,17]:

$$\% = \frac{(C_0 - C_t)}{C_0}\,100 \quad (2)$$

For equilibrium conditions, C_t in Eq. (2) was replaced by C_e. All experimental values were reported as mean ± SD.

2.4. Adsorption modeling and statistical analysis

2.4.1. *Kinetic and diffusion modeling*

The kinetic experiments were conducted under the RSM–ANN-optimized conditions previously established in our earlier study [14], namely C_0 = 42.65 mg/L, an HSCA dosage of 1.29 g/L, T = 30.4 °C, and pH 3.0. The resulting kinetic data were evaluated using the pseudo-first-order (PFO) and pseudo-second-order (PSO) kinetic models [18,19]. Because the experiments were performed at a single initial MO concentration, the estimated kinetic parameters were considered specific to the investigated experimental conditions.

The nonlinear PFO model is given by Eq. (3) [18]:

$$q_t = q_e(1 - e^{-k_1 t}) \quad (3)$$

where q_t and q_e are the adsorption capacities at time t and equilibrium, respectively (mg/g), and k_1 is the PFO rate constant (min^{-1}).

The nonlinear PSO model is given by Eq. (4) [19]:

$$q_t = \frac{k_2 q_e^2 t}{(1 + k_2 q_e t)} \quad (4)$$

where k_2 is the PSO rate constant (g/mg min).

The PFO and PSO models were evaluated using linearized, unweighted nonlinear, and weighted nonlinear regression approaches. Linear regression was performed using the conventionally transformed forms of the models, whereas nonlinear regression was applied directly to the original $q_t - t$ data using Eq. (3) and Eq. (4). For weighted nonlinear regression, inverse-variance weighting was applied to account for the experimental variability associated with each mean q_t value [20], with the weight of the i-th observation defined as $w_i = 1/SD_i^2$, where SD_i is the experimental standard deviation associated with the corresponding mean q_t value.

The contribution of mass-transfer processes to MO uptake was further evaluated using the Weber–Morris intraparticle diffusion and Boyd diffusion models [21–23].

The Weber–Morris model is given by Eq. (5) [21]:

$$q_t = k_{id} t^{0.5} + C \quad (5)$$

where k_{id} is the apparent intraparticle diffusion rate constant (mg/g $min^{0.5}$), and C is the intercept conventionally associated with boundary-layer and external mass-transfer effects.

The q_t versus $t^{0.5}$ profile was evaluated using a three-region representation based on changes in slope and the distribution of the experimental observations across successive adsorption stages. For Stage I (5–60 min), the intercept was constrained to C=0, consistent with the physical initial condition q_t=0 at t=0. Stages II and III were fitted with freely estimated intercepts. The regional Weber–Morris fits were evaluated using inverse-variance weighting based on the experimental SD values.

For the Boyd analysis, the fractional MO uptake, F, was calculated using Eq. (6) [22]:

$$F = \frac{q_t}{q_{e,exp}} \quad (6)$$

where $q_{e,exp}$ is the experimentally observed equilibrium adsorption capacity. The Boyd time function, B_t, was calculated using **Eqs. (7)** and **(8)** [22,23]:

$$B_t = \left[\sqrt{\pi} - \sqrt{\pi - \frac{\pi^2 F}{3}}\right]^2 \quad \text{for } F \leq 0.85 \quad (7)$$

$$B_t = -0.4977 - \ln(1 - F) \quad \text{for } F > 0.85 \quad (8)$$

The t = 0 observation was treated as the experimental baseline and was excluded from the transformed Boyd regression. The equilibrium observation at 360 min, for which F = 1, was also excluded because the Boyd transformation becomes undefined at F = 1. Thus, the Boyd analysis was performed using the remaining 11 observations. The $B_t - t$ relationship was evaluated using ordinary least-squares graphical regression, while an uncertainty-weighted regression was additionally applied as a sensitivity analysis. The corresponding slopes and intercepts were estimated from these regressions.

2.4.2. *Equilibrium isotherm modeling*

The equilibrium adsorption data obtained at each temperature were evaluated using the Freundlich, Langmuir, and Redlich–Peterson isotherm models [24–26].

The Freundlich model is given by Eq. (9) [24]:

$$q_e = K_F C_e^{1/n_F} \quad (9)$$

where K_F is the Freundlich capacity constant [(mg/g)(L/mg)$^{(1/n_F)}$] and n_F is the Freundlich adsorption-intensity parameter.

The Langmuir model is given by Eq. (10) [25]:

$$q_e = \frac{q_m K_L C_e}{(1 + K_L C_e)} \quad (10)$$

where q_m is the model-predicted monolayer adsorption capacity (mg/g) and K_L is the Langmuir affinity constant (L/mg).

The Redlich–Peterson model is given by Eq. (11) [26]:

$$q_e = \frac{K_{RP} C_e}{1 + a_{RP} C_e^{\beta}} \quad (11)$$

where K_{RP} and a_{RP} are the Redlich–Peterson constants and β is the model exponent constrained to $0 < \beta \leq 1$. When β approaches unity, the Redlich–Peterson equation exhibits Langmuir-like behavior.

The Freundlich and Langmuir models were evaluated using linearized, unweighted nonlinear, and weighted nonlinear regression approaches, whereas the Redlich–Peterson model was evaluated using unweighted and weighted nonlinear regression. Linearized fitting was performed using the conventional transformed forms of the Freundlich and Langmuir equations, whereas nonlinear regression was applied directly to the original $C_e - q_e$ data using **Eqs. (9) – (11)**.

For weighted nonlinear regression, inverse-variance weighting was applied to account for the experimental variability associated with each mean q_e value [18], with the weight of the i^{th} observation defined as $w_i = 1/SD_i^2$, where SD_i is the experimental standard deviation associated with the corresponding mean q_e value. C_e was treated as the predictor variable in the nonlinear least-squares procedure.

2.4.3. Apparent thermodynamic analysis

The temperature dependence of MO adsorption was evaluated using the apparent equilibrium constant, K_C, calculated from the equilibrium concentration ratio according to Eq. (12) [17,27]:

$$K_C = \frac{(C_0 - C_e)}{C_e} \tag{12}$$

The apparent Gibbs free energy change was calculated using Eq. (13) [17,27]:

$$\Delta G_{app} = -RTlnK_C \tag{13}$$

where ΔG_{app} is the apparent Gibbs free energy change (J/mol), R is the universal gas constant (8.314 J/mol K), and T is the absolute temperature (K).

The apparent enthalpy and entropy changes were estimated using the Van't Hoff relationship given in Eq. (14) [17,27]:

$$lnK_C = -\frac{\Delta H_{app}}{RT} + \frac{\Delta S_{app}}{R} \tag{14}$$

where ΔH_{app} and ΔS_{app} are the apparent enthalpy and entropy changes, respectively. The Van't Hoff relationship in Eq. (14) was established by regressing lnKc against $1/T$. When $1000/T$ was used for graphical presentation, the corresponding scaling factor was included when calculating ΔH_{app} from the fitted slope.

The experimental uncertainty in C_e was propagated through Eq. (12) to K_C and subsequently to lnK_C. The resulting uncertainty in lnK_C was used to construct error bars and determine the inverse-variance weights applied in the weighted Van't Hoff regression.

Because K_C in Eq. (12) was calculated from a concentration ratio rather than from a dimensionless activity-based standard-state equilibrium constant, the resulting ΔG_{app}, ΔH_{app}, and ΔS_{app} values were interpreted as conditional apparent thermodynamic parameters valid under the investigated experimental conditions. They were not interpreted as strict standard-state thermodynamic quantities.

The linear Van't Hoff treatment based on Eq. (14) additionally assumes that the apparent enthalpy and entropy remain approximately constant over the investigated temperature interval. Given the limited number of experimental temperatures, the resulting ΔH_{app} and ΔS_{app} values were regarded as average apparent parameters over the studied range. Their interpretation was based on the direction and consistency of the observed temperature dependence rather than solely on the numerical values of the fitted slope and intercept.

2.4.4. Statistical analysis and model comparison

Model parameters were estimated using ordinary or weighted least-squares regression, as appropriate. Experimental measurements were reported as mean ± standard deviation (SD), whereas fitted model parameters were reported as estimate ± standard error (SE).

Residuals were defined according to Eq. (15):

$$e_i = y_{i,exp} - y_{i,cal} \tag{15}$$

where e_i is the residual associated with observation i, and $y_{i,exp}$ and $y_{i,cal}$ are the corresponding experimental and model-calculated response values, respectively. Accordingly, the residuals of the kinetic, diffusion, and equilibrium models were calculated as $q_{exp} - q_{cal}$. Boyd residuals were calculated as $B_{t,exp} - \mathbf{B_{t,cal}}$, whereas Van't Hoff residuals were calculated as $lnK_{C,exp} - lnK_{C,cal}$.

Goodness of fit was evaluated using the coefficient of determination (R^2), root mean square error (RMSE), mean absolute error (MAE), and chi-square statistic (χ^2). R^2, RMSE, and MAE were calculated according to **Eqs. (16) – (18)**, respectively:

$$R^2 = 1 - \left[\frac{\sum(y_{i,exp} - y_{i,cal})^2}{\sum(y_{i,exp} - \bar{y}_{i,exp})^2}\right] \tag{16}$$

$$\text{RMSE} = \sqrt{\frac{1}{N}\sum(y_{i,exp} - y_{i,cal})^2} \tag{17}$$

$$\text{MAE} = \frac{1}{N}\sum|y_{i,exp} - y_{i,cal}| \tag{18}$$

where N is the number of experimental observations and $\bar{y}_{i,exp}$ is the mean experimental response. For uncertainty-weighted analyses, χ^2 was calculated using Eq. (19):

$$\chi^2 = \sum \left[\frac{(y_{i,exp} - y_{i,cal})}{\sigma_i} \right]^2 \quad (19)$$

where σ_i is the experimental SD associated with observation i. Higher R^2 values and lower RMSE, MAE, and χ^2 values indicate closer agreement between the experimental and model-calculated responses. However, these goodness-of-fit measures were not used individually to determine the preferred model.

To provide an objective comparison among competing nonlinear models fitted to the same dataset, the Akaike information criterion (AIC), small-sample-corrected Akaike information criterion (AICc), and Bayesian information criterion (BIC) were calculated according to **Eqs. (20) – (22)**, respectively [28,29]. AIC provides an information-theoretic balance between goodness of fit and model complexity, whereas BIC applies a sample-size-dependent penalty for increasing model complexity.

$$\mathrm{AIC} = 2p - 2ln(L) \quad (20)$$

$$\mathrm{AICc} = \mathrm{AIC} + \left[\frac{2p(p+1)}{(N-p-1)} \right] \quad (21)$$

$$\mathrm{BIC} = p\ln(N) - 2\,ln(L) \quad (22)$$

where L is the maximized likelihood, p is the number of estimated model parameters, and N is the number of observations. Because the number of observations was relatively limited compared with the number of fitted parameters, AICc in Eq. (21) was emphasized in the model-selection procedure.

For each candidate model, ΔAICc was calculated according to Eq. (23):

$$\Delta_i = \mathrm{AICc}_i - \mathrm{AICc}_{min} \quad (23)$$

where AICc_i is the AICc value of model i and AICc_{min} is the lowest AICc value among the candidate models fitted to the same dataset. The corresponding Akaike weight was then calculated using Eq. (24):

$$w_i = \frac{e^{(-\Delta_i/2)}}{\sum_j e^{(-\Delta_j/2)}} \quad (24)$$

where the denominator represents the sum over all candidate models included in the corresponding comparison. The Akaike weight in Eq. (24) was interpreted as the relative statistical support for each model within the specified candidate set. Therefore, the weight values were not interpreted independently of the models included in that candidate set.

AIC, AICc, BIC, ΔAICc, and Akaike weights were compared only among models fitted to the same observations, response variable, and error structure. Consequently, information criteria obtained from transformed linear fits were not directly compared with those obtained from nonlinear models fitted to the original response scale. Similarly, weighted and unweighted nonlinear fits were evaluated separately under their respective error assumptions.

Residual normality was assessed using the Shapiro–Wilk test [30], whereas randomness of the ordered residual sequence was evaluated using the Wald–Wolfowitz runs test at α = 0.05 [31]. The Shapiro–Wilk procedure was originally developed to assess departure from normality, while the runs-based approach was used here to assess whether the signs of the ordered residuals showed evidence of a systematic sequence. Because the individual kinetic and equilibrium datasets contained relatively few observations, these tests were interpreted together with the corresponding residual plots and other model-evaluation criteria rather than as stand-alone evidence of model adequacy.

Final model evaluation was based collectively on parameter estimates and their SE values, residual behavior, R^2, RMSE, MAE, χ^2, AICc, BIC, ΔAICc, and Akaike weights. Statistical preference for a model was interpreted only as evidence of superior descriptive performance within the evaluated candidate set and was not considered direct evidence of a particular adsorption mechanism. All calculations, parameter estimations, uncertainty analyses, statistical tests, and graphical outputs were performed in Google Colaboratory (Google LLC, Mountain View, CA, USA) using Python 3.12.13 (Python Software Foundation, USA), NumPy 2.0.2, pandas 2.2.2, SciPy 1.16.3, and Matplotlib 3.10.0 [32,33].

2.5. Physicochemical characterizations

2.5.1. *Textural characterization*

The textural properties of pristine and MO-loaded HSCA were determined by N_2 adsorption–desorption analysis at 77.30 K using an Autosorb-6B surface area and pore-size analyzer (Quantachrome Corporation, Boynton Beach, FL, USA). Before analysis, the samples were degassed under vacuum at 120.0 °C for 3 h. The adsorption–desorption isotherms were recorded over a relative pressure (P/P_0) range of 0.0002–0.99. The specific

surface area was calculated using the multipoint BET method. The micropore surface area, external surface area, and micropore volume were determined using the *t*-plot method. The cumulative mesopore volume and modal mesopore diameter were calculated from the desorption branch using the BJH method. The pore-size distribution was evaluated using the NLDFT equilibrium model with an N_2-on-carbon kernel, assuming slit-shaped micropores and cylindrical mesopores.

2.5.2. *FE-SEM and EDX analysis*

The surface morphology and elemental composition of pristine and MO-loaded HSCA were examined using a field-emission scanning electron microscope equipped with an energy-dispersive X-ray spectroscopy detector (FE-SEM–EDX; MIRA3 XMU, TESCAN, Brno, Czech Republic). The dried samples were mounted on conductive carbon tape and coated with a thin layer of gold before analysis. FE-SEM images were acquired at magnifications ranging from 20,000 × to 200,000 × to examine the surface morphology and visible pore features of the samples. EDX spectra were collected from selected regions to evaluate their semi-quantitative elemental composition. Any Au signal detected in the EDX spectra was attributed to the conductive coating and excluded from the compositional interpretation.

2.5.3. *X-ray diffraction analysis*

The crystalline and amorphous structural features of pristine MO, pristine HSCA, and MO-loaded HSCA were examined by XRD using a MiniFlex 600 diffractometer (Rigaku Corporation, Tokyo, Japan) with Cu Kα radiation (λ = 1.5406 Å). Measurements were performed at 40 kV and 15 mA over a 2θ range of 5–90°, using a step size of 0.01° and a scanning rate of 3.00°/min. The diffraction patterns were compared to assess changes in the structural features of HSCA after MO adsorption.

2.5.4. *Surface charge characterization of HSCA*

The surface charge behavior of HSCA was evaluated by determining both the point of zero charge (pH_{PZC}) and the pH-dependent zeta potential. The pH_{PZC} was determined using the pH drift method. Briefly, 10 mM NaCl solutions were prepared using deionized water, and 100 mL of each electrolyte solution was adjusted to the desired initial pH value using 100 mM HCl or NaOH. HSCA was then added to each solution at an adsorbent loading of 1.29 g/L, and the suspensions were agitated at 225 rpm and 25.0 °C for 24 h to allow equilibration between the solid surface and the electrolyte solution. After equilibration, the final pH values were measured, and the pH change was calculated according to Eq. (25):

$$\Delta pH = pH_{final} - pH_0 \quad (25)$$

where pH_0 and pH_{final} are the initial and final pH values of the suspension, respectively. The pH_{PZC} value was determined from the intersection of the ΔpH versus pH_0 curve with the line corresponding to ΔpH = 0.

Zeta potential measurements were performed to further evaluate the pH-dependent electrokinetic behavior of HSCA. Measurements were carried out using an Electrokinetic Analyzer (SurPASS-Type A, Anton Paar GmbH, Graz, Austria) in 10 mM NaCl electrolyte solution [33]. The pH of the electrolyte was adjusted over the selected pH range using dilute HCl or NaOH solutions. Zeta potential values were calculated from streaming potential measurements using the classical Smoluchowski equation. The isoelectric point, pH_{IEP}, was determined as the pH value at which the zeta potential became zero. The pH_{PZC} and zeta-potential measurements were considered complementary indicators of the surface-charge behavior of HSCA.

2.5.5. *Fourier-transform infrared spectroscopy*

FTIR spectroscopy was performed to identify the characteristic functional groups of MO and HSCA and to evaluate the spectral changes associated with MO adsorption onto the HSCA surface. Spectra were recorded for pristine MO, pristine HSCA, and MO-loaded HSCA obtained after the adsorption process. Prior to FTIR analysis, the solid samples were dried and finely ground with spectroscopic-grade KBr. The resulting mixtures were pressed into transparent pellets and analyzed using an FTIR spectrometer (Spectrum 100 Model, Perkin Elmer, Inc., Norwalk, CT, USA).

All spectra were collected at room temperature over the wavenumber range of 580–4000 cm^{-1} with a spectral resolution of 4 cm^{-1}. The FTIR spectra were evaluated to identify vibrational bands that may be associated with oxygen-containing surface functional groups, aromatic structures, azo-related vibrations, and sulfonate-containing moieties. Changes in band position, band intensity, or band shape after adsorption were evaluated to support the interpretation of possible interactions between MO and HSCA. Particular attention was given to the hydroxyl, aromatic C=C, C–N/azo-related, and sulfonate-associated regions, since these spectral regions can provide supporting evidence for possible hydrogen bonding, π–π interactions, and electrostatic interactions between MO and the HSCA surface.

2.6. Quantum chemical calculations and molecular-level adsorption analysis

Quantum chemical calculations were performed to investigate possible molecular-level interactions

between MO and the HSCA model surface. Since the adsorption experiments were conducted under acidic conditions at pH 3.0, MO was modeled in its protonated form. Protonation was introduced at an azo nitrogen atom, while the sulfonate group remained deprotonated, resulting in an overall neutral zwitterionic species (charge = 0, singlet state). The unprotonated and azo-N-protonated MO structures are shown in Fig. 2. The optimized protonated MO structure had approximate molecular dimensions of 1.469 nm in length and 0.437 nm in width.

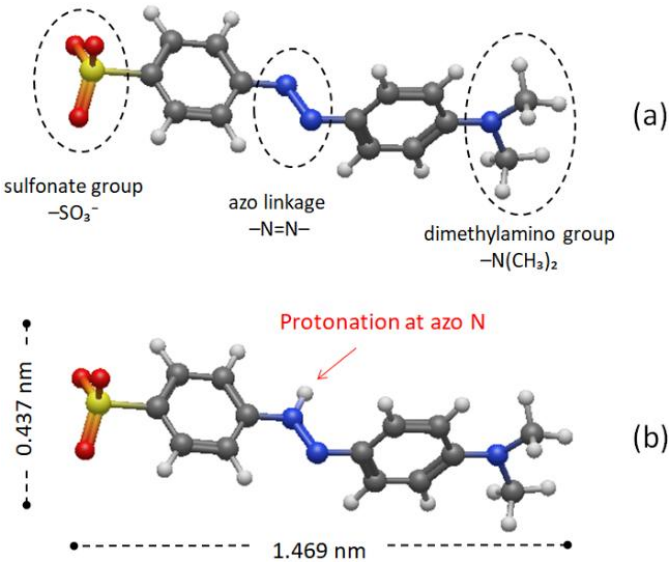


Figure 2. Molecular structures of methyl orange: (a) unprotonated MO and (b) azo-N-protonated MO used in the DFT calculations

The HSCA surface was represented by a finite oxygen-functionalized polyaromatic carbon cluster ($C_{55}H_{18}O_5$; charge = 0, singlet state), which was used as a simplified model of representative aromatic/graphitic domains and oxygen-containing surface functionalities of HSCA. Because the actual HSCA surface is chemically and structurally heterogeneous, the finite cluster was not intended to reproduce the complete adsorbent surface but rather to provide a computationally tractable local adsorption environment for examining possible MO–surface interactions.

A single initial MO–HSCA adsorption configuration was investigated. Protonated MO was initially positioned approximately parallel to the aromatic carbon surface, with an initial intermolecular separation of approximately 3.2–3.5 Å. Possible intermolecular contacts involving the sulfonate region of MO and oxygen-containing functionalities of the HSCA model were also considered when constructing the initial complex geometry. Accordingly, the optimized MO–HSCA complex was regarded as a local minimum associated with the investigated starting configuration and was not assumed to represent the global minimum among all possible adsorption geometries. All quantum chemical calculations were performed using Gaussian 16 Revision C.01 (Gaussian, Inc., Wallingford, CT, USA) [34].

Geometry optimizations of protonated MO, the HSCA cluster, and the MO–HSCA adsorption complex were performed within the framework of DFT using the B3LYP exchange–correlation functional and the def2-SVP basis set. Grimme's D3 empirical dispersion correction with Becke–Johnson damping (GD3BJ) was included to account for dispersion interactions.

Solvent effects were represented using the Solvation Model based on Density (SMD) with water as the solvent. Geometry optimizations were performed without symmetry constraints using tight convergence criteria and an ultrafine integration grid. Harmonic vibrational frequency calculations were subsequently performed at the same B3LYP/def2-SVP-GD3BJ/SMD(water) level. The absence of imaginary frequencies confirmed that the optimized structures corresponded to local minima on their respective potential-energy surfaces. Frequency calculations were also used to obtain zero-point-energy corrections and thermal contributions to enthalpy, entropy, and Gibbs free energy at 298.15 K and 1 atm.

To improve the description of the electronic energies, single-point calculations were subsequently performed on the optimized geometries using the larger 6-311+G(d,p) basis set while retaining the B3LYP functional, GD3BJ dispersion correction, and SMD water solvation model. The model-level adsorption energy, ΔEads, was calculated using the supermolecule approach according to Eq. (26) [35]:

$$\Delta E_{\text{ads}} = E_{\text{complex}} - (E_{\text{MO}} + E_{\text{HSCA}}) \quad (26)$$

where Ecomplex, EMO, and EHSCA are the electronic energies of the MO–HSCA complex, protonated MO, and HSCA cluster, respectively. Negative ΔEads values indicate energetically favorable complex formation within the adopted cluster model.

Basis set superposition error (BSSE) correction was not applied to the reported adsorption energy. Therefore, the calculated ΔEads was interpreted as a model-level energetic quantity within the adopted computational protocol, and the possible influence of the absence of BSSE correction was considered when interpreting its magnitude.

DFT-derived thermodynamic changes associated with the formation of the model MO-HSCA complex, including ΔHads, ΔGads, and ΔSads, were calculated from the differences between the corresponding

Table 1. Kinetic model parameters and statistical criteria for MO adsorption onto HSCA using different regression approaches.

Statistic	Linearized		Unweighted nonlinear		Weighted nonlinear	
	PFO	PSO	PFO	PSO	PFO	PSO
q_e ± SE (mg/g)	34.817	40.660	32.624±0.532	40.970±1.403	32.545±0.083	38.986±0.215
Rate constant ± SE k_1 (min^{-1})	1.498×10^{-2}		$(1.275\pm0.059) \times 10^{-2}$		$(1.274\pm 0.021) \times 10^{-2}$	
k_2 (g/mg min)		3.032×10^{-4}		$(3.040\pm0.388) \times 10^{-4}$		$(3.587\pm0.112) \times 10^{-4}$
q_e bias (%)	8.18	26.34	1.37	27.30	1.12	21.14
R^2	0.9389	0.9907	0.9955	0.9912	0.9955	0.9890
RMSE (mg/g)	2.68	1.05	0.73	1.02	0.73	1.13
MAE (mg/g)	2.37	0.88	0.52	0.90	0.51	0.99
χ^2w	1904.38	233.93	41.72	334.47	40.12	143.25
AICc	—	—	31.78	39.86	41.94	145.08
ΔAICc	—	—	<0.0001	8.08	<0.0001	103.13
Akaike weight	—	—	0.9827	0.0173	1.0000	<0.0001
BIC	—	—	31.42	39.49	41.58	144.71
Shapiro–Wilk p	—	—	0.34	0.68	0.27	0.63
Runs-test p	—	—	0.92	0.25	1.00	0.23

thermodynamic quantities of the optimized complex and the isolated components according to Eq. (27) [35]:

$$\Delta X_{\mathrm{ads}} = X_{\mathrm{complex}} - (X_{\mathrm{MO}} + X_{\mathrm{HSCA}}) \quad (27)$$

where X represents H, G, or S. These quantities were obtained from the frequency calculations at 298.15 K and 1 atm and describe the thermodynamic change associated with the formation of the investigated finite cluster complex. They were not directly equated with the experimentally derived apparent thermodynamic parameters (ΔGapp, ΔHapp, and ΔSapp), which were obtained independently from the equilibrium adsorption data.

Natural bond orbital (NBO) analysis was performed at the single-point calculation level to evaluate intermolecular donor–acceptor interactions, charge-transfer contributions, and second-order perturbation stabilization energies, E(2). Non-covalent interaction (NCI) analysis was additionally performed using the reduced density gradient (RDG) approach to visualize weak intermolecular interactions within the optimized MO–HSCA complex. Electron-density distributions were obtained from Gaussian-generated formatted checkpoint (.fchk) files. The RDG and sign(λ_2)ϱ functions were calculated using Multiwfn (Version 2026.1.12) [36,37], and the resulting RDG isosurfaces were visualized using Visual Molecular Dynamics (VMD, version 1.9.3; University of Illinois at Urbana-Champaign, Urbana, IL, USA) [38]. The NBO and NCI analyses were used as complementary molecular-level tools for characterizing possible donor–acceptor, attractive, dispersion-dominated, and steric interactions within the investigated model complex.

3. 3. Results and discussion

3.1. Kinetic and diffusion modeling

The adsorption kinetics of MO onto HSCA were evaluated using the PFO and PSO models, and the corresponding parameters and statistical criteria are summarized in Table 1. The fitted curves and standardized residuals obtained using the different regression approaches are presented in Fig. 3. The experimental adsorption capacity increased rapidly during the initial period and gradually approached an equilibrium value of 32.183 ± 0.086 mg/g at 360 min. Preliminary agitation-speed experiments showed that no clear equilibrium plateau was reached at 125 rpm, with an adsorption capacity of 13.635 ± 0.741 mg/g after 360 min, whereas 325 rpm accelerated the approach to equilibrium and yielded a 360-min adsorption capacity of 32.964 ± 0.010 mg/g. Thus, increasing the agitation speed from 225 to 325 rpm increased the 360-min capacity by only 2.43%. Because higher agitation can enhance external mass transfer but requires greater mechanical energy input, 225 rpm was selected as the working agitation speed [39,40]. Because the kinetic experiments were conducted at a single initial MO concentration of 42.65 mg/L, the estimated kinetic parameters describe the investigated conditions and should not be regarded as concentration-independent kinetic constants.

Linearization affected the estimated parameters and goodness-of-fit statistics, particularly for the PFO model.

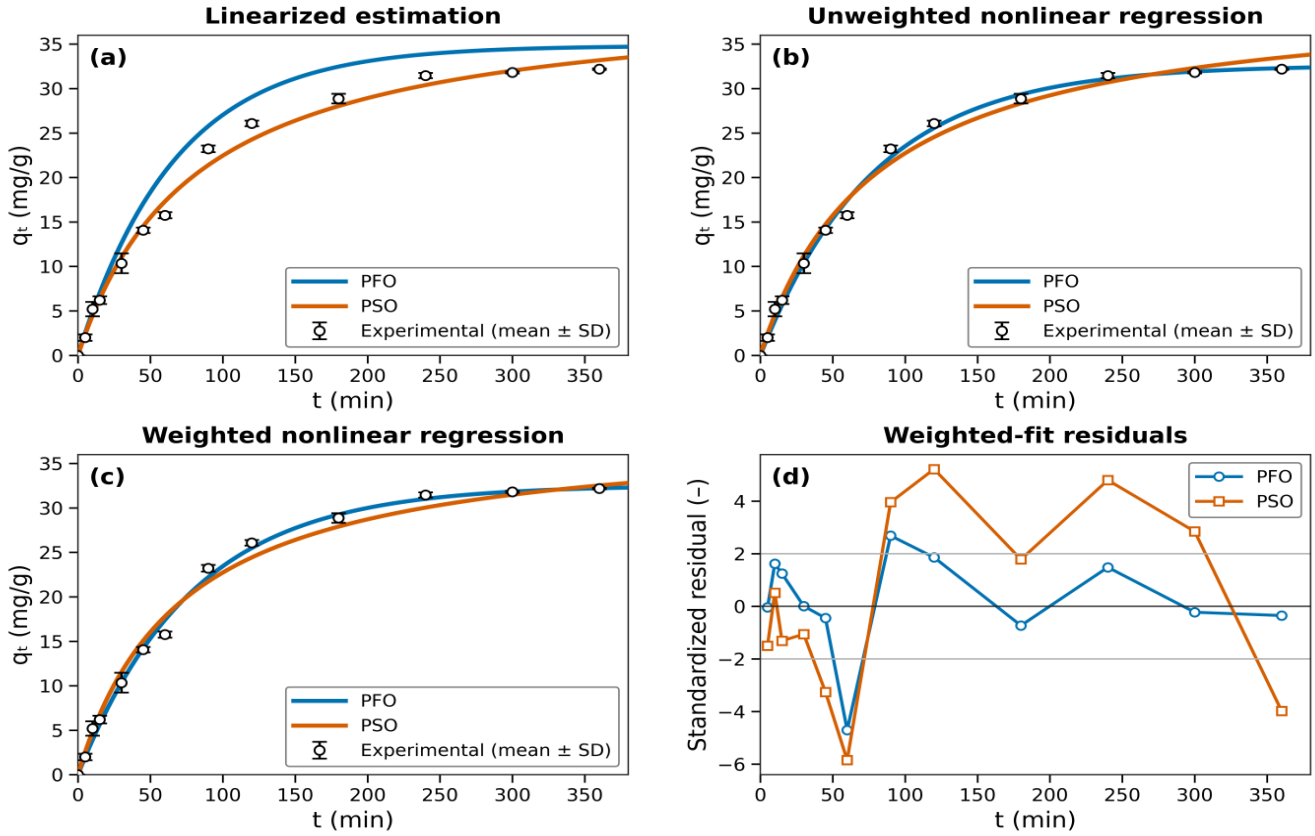


Figure 3. PFO and PSO kinetic fits and standardized residuals for MO adsorption onto HSCA using different regression approaches

The linearized PFO fit produced an original-space R^2 of 0.9389 and an RMSE of 2.68 mg/g, whereas direct nonlinear regression considerably improved agreement with the experimental data. For the unweighted nonlinear analysis, the PFO model yielded q_e = 32.624 ± 0.532 mg/g and k_1 = (1.275 ± 0.059) × 10^{-2} min^{-1}, with R^2 = 0.9955, RMSE = 0.73 mg/g, and MAE = 0.52 mg/g. The corresponding PSO model yielded q_e = 40.970 ± 1.403 mg/g and k_2 = (3.040 ± 0.388) × 10^{-4} g/mg min, with R^2 = 0.9912 and RMSE = 1.02 mg/g.

The statistical preference for the PFO model was also supported by the information criteria. For the unweighted nonlinear fits, PFO showed lower AICc and BIC values than PSO, with ΔAICc = 8.08 and Akaike weights of 0.9827 and 0.0173 for PFO and PSO, respectively. In addition, the PFO-predicted equilibrium capacity differed from the experimental value by only 1.37%, whereas the PSO estimate was 27.30% higher. The weighted nonlinear analysis produced the same model ranking: PFO predicted q_e = 32.545 ± 0.083 mg/g, corresponding to a bias of 1.12%, whereas PSO predicted

Table 2. Weber–Morris and Boyd diffusion-model parameters and statistical evaluation for MO adsorption onto HSCA.

Weber–Morris model			
Statistic / parameter	**Stage I**	**Stage II**	**Stage III**
Time range (min)	5–60	90–180	240–360
k_{id} ± SE (mg/g $min^{0.5}$)	1.984 ± 0.030	1.458 ± 0.167	0.219 ± 0.067
C ± SE (mg/g)	0 (fixed)	9.725 ± 1.826	28.027 ± 1.219
R^2	0.9285	0.9727	0.9949
RMSE (mg/g)	1.31	0.38	0.02
MAE (mg/g)	1.11	0.38	0.02
χ^2w	65.10	2.88	0.03
Boyd model			
Statistic / parameter	**OLS graphical analysis**	**Uncertainty-weighted sensitivity**	
n	11	11	
B ± SE (min^{-1})	(1.372 ± 0.073) × 10^{-2}	(6.462 ± 0.829) × 10^{-3}	
Intercept ± SE	−0.305 ± 0.101	−0.032 ± 0.009	
R^2	0.9751	0.5880	
RMSE (mg/g)	0.21	0.85	
MAE (mg/g)	0.18	0.49	
χ^2w	—	246.31	

Note: *For Stage I, C was fixed at 0 and was therefore not estimated from the regression; accordingly, no SE is applicable to this parameter.*

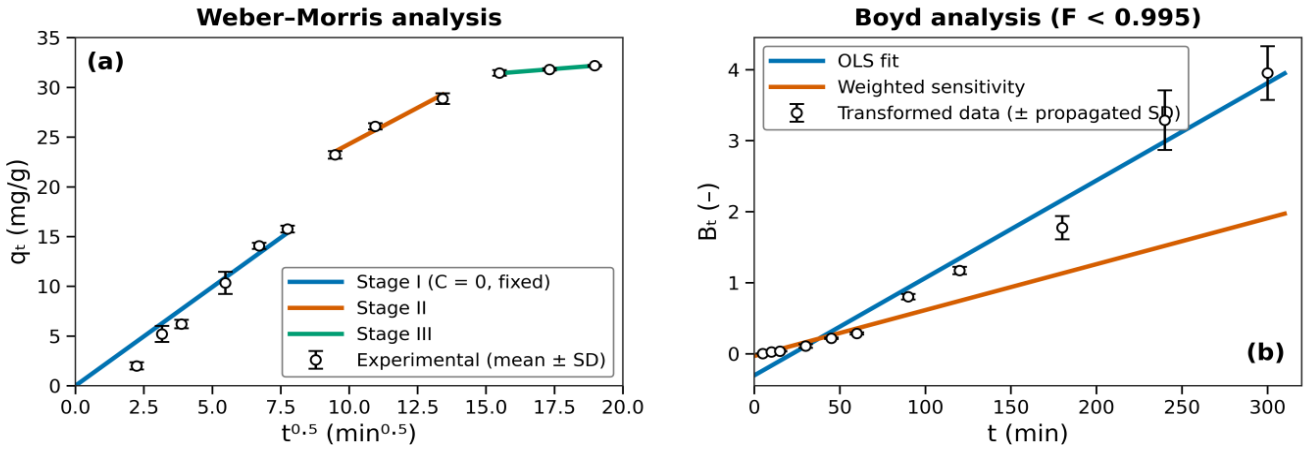


Figure 4. Weber–Morris and Boyd diffusion analyses for MO adsorption onto HSCA: (a) three-stage Weber–Morris fit with $C = 0$ for Stage I and (b) Boyd analysis.

q_e = 38.986 ± 0.215 mg/g, corresponding to a bias of 21.14%. The difference between the PFO- and PSO-derived q_e values was therefore interpreted as a model-dependent fitting outcome associated with their different mathematical structures and asymptotic behavior rather than as evidence of different experimental equilibrium capacities.

Although weighting did not substantially improve R^2 or RMSE, it incorporated the experimental SD values and reduced the uncertainty of the estimated PFO parameters. For example, the SE of the PFO q_e estimate decreased from 0.532 mg/g for the unweighted fit to 0.083 mg/g for the weighted fit. The Shapiro–Wilk and runs-test results for the nonlinear PFO residuals were not significant at $\alpha = 0.05$, consistent with the absence of strong evidence for non-normality or a systematic residual sequence. Accordingly, weighted regression was retained as an uncertainty-sensitive complementary analysis rather than as a procedure that changed the overall kinetic conclusion. Collectively, the results indicate that the nonlinear PFO model provided the most appropriate empirical description of the kinetic data under the investigated conditions. This statistical preference, however, was not interpreted as direct evidence of a specific physical or chemical adsorption mechanism [41,42].

The diffusion-model parameters and statistical results are summarized in Table 2, and the corresponding Weber–Morris and Boyd analyses are shown in Fig. 4. The three-stage Weber–Morris representation consisted of an initial region spanning 5–60 min, a second region covering 90–180 min, and a final region extending from 240 to 360 min. To maintain consistency with the physical initial condition $q_t = 0$ at $t = 0$, the Stage I intercept was constrained to $C = 0$. The resulting apparent intraparticle-diffusion rate constant for Stage I was 1.984±0.030 mg/g min$^{0.5}$, followed by 1.458 ± 0.167 mg/g min$^{0.5}$ for Stage II and 0.219±0.067 mg/g min$^{0.5}$ for Stage III. The progressive decrease in k_{id} is consistent with initially rapid uptake followed by slower transport within the porous structure and gradual approach to equilibrium [21]. The Stage I constrained fit yielded R^2=0.9285, indicating that the earliest adsorption region was not perfectly represented by a single linear intraparticle-diffusion relationship.

e Weber–Morris fit with $C = 0$ for Stage I and (b) Boyd analysis.

In the revised Weber–Morris analysis, the Stage I intercept was constrained to C=0 to satisfy the physical initial condition q_t=0 at t=0. The constrained Stage I fit yielded k_{id}=1.984±0.030 mg/g min$^{0.5}$, with R^2 = 0.9285, RMSE = 1.31 mg/g, MAE = 1.11 mg/g, and $\chi^2 w$ = 65.10. In contrast, Stages II and III retained positive fitted intercepts of 9.725±1.826 and 28.027 ± 1.219 mg/g, respectively. Thus, although intraparticle diffusion contributes to the uptake process, the overall Weber–Morris behavior does not support exclusive intraparticle-diffusion control throughout the entire adsorption period.

The Boyd analysis was used as a complementary diagnostic of diffusion behavior. Of the 13 kinetic observations, t = 0 was treated as the experimental baseline and the 360-min observation was excluded because $F = 1$ makes the Boyd transformation undefined; thus, 11 observations were included in the regression. The OLS graphical fit yielded B = (1.372 ± 0.073) × 10^{-2} min^{-1} with an intercept of −0.305 ± 0.101 and R^2 = 0.9751. In contrast, the uncertainty-weighted sensitivity analysis yielded B = (6.462 ± 0.829) × 10^{-3} min^{-1}, an intercept of −0.032 ± 0.009, and R^2 = 0.5880. The non-zero Boyd intercept and the sensitivity of the fit to uncertainty weighting do not provide robust evidence for exclusive particle-diffusion control. Taken together, the Weber–Morris and Boyd results are consistent with successive and overlapping contributions from external mass transfer, intraparticle diffusion, and equilibration rather than a single rate-controlling diffusion mechanism [22].

3.2. Equilibrium isotherm modeling and fitting evaluation

The equilibrium adsorption behavior of MO onto HSCA was evaluated at 10.0, 20.0, 30.4, and 40.0 °C using the

Freundlich, Langmuir, and Redlich–Peterson isotherm models. Freundlich and Langmuir were evaluated using linearized, unweighted nonlinear, and weighted nonlinear regression, whereas Redlich–Peterson was evaluated using unweighted and weighted nonlinear regression. The corresponding isotherm fits are presented in Fig. 5. The linearized Freundlich and Langmuir results are summarized in Table 3, while the unweighted and weighted nonlinear results are presented in Table 4 and Table 5, respectively. Model performance was evaluated collectively using parameter estimates and their associated SE values, R2, RMSE, MAE, χ2, AICc, BIC, and residual behavior rather than relying on R2 alone, consistent with previous recommendations for adsorption-isotherm evaluation [43–47]. Sips, Tóth, Temkin, and Dubinin–Radushkevich models were also examined during preliminary screening. Temkin and Dubinin–Radushkevich showed poorer agreement with the experimental data, whereas Sips and Tóth provided good fits in some cases but exhibited parameter-instability and identifiability limitations, including excessively large or boundary-sensitive saturation-capacity estimates. Therefore, the final detailed comparison was restricted to Freundlich, Langmuir, and Redlich–Peterson.

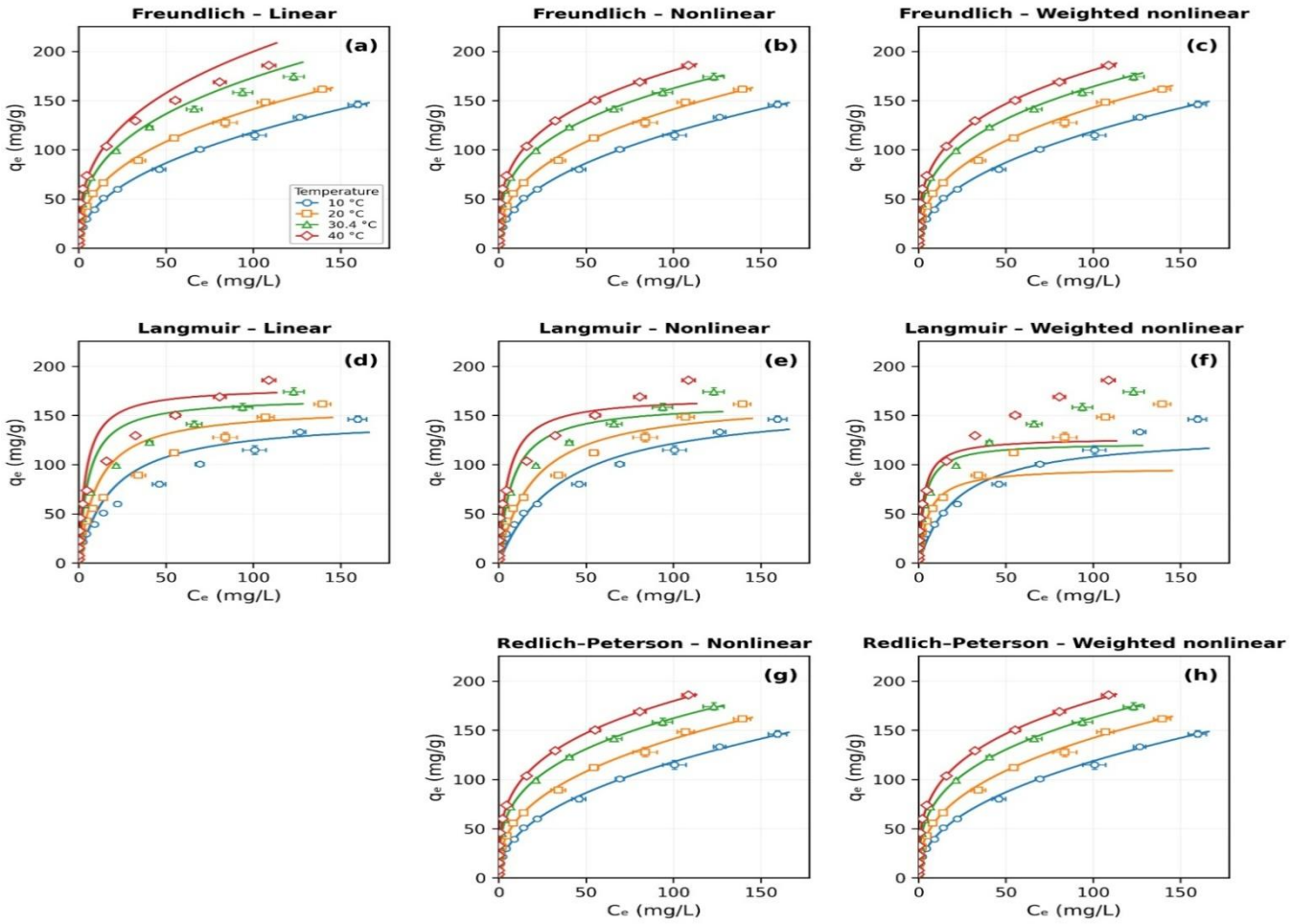


Figure 5. Freundlich, Langmuir, and Redlich–Peterson isotherm fit for MO adsorption onto HSCA at different temperatures using linear, nonlinear, and weighted nonlinear regression approaches

The linearized results in Table 3 showed that Freundlich provided a markedly better representation of the equilibrium data than Langmuir at all investigated

Table 3. Linearized Freundlich and Langmuir isotherm parameters and fitting statistics for MO adsorption onto HSCA at different temperatures.

T	Model	Parameters	R^2	RMSE	MAE	χ^2
10.0	Freundlich	K_F = 15.217 n_F = 2.247	0.9988	1.61	1.10	0.38
	Langmuir	q_m = 147.858 K_L = 0.054	0.9315	12.31	10.45	84.33
20.0	Freundlich	K_F = 24.196 n_F = 2.607	0.9985	2.06	1.33	0.54
	Langmuir	q_m = 158.853 K_L = 0.095	0.9168	15.18	12.85	233.05
30.4	Freundlich	K_F = 35.412 n_F = 2.896	0.9897	5.82	4.54	4.62
	Langmuir	q_m = 168.703 K_L = 0.187	0.9163	16.64	13.526	473.66
40.0	Freundlich	K_F = 41.539 n_F = 2.929	0.9783	9.06	7.06	10.53
	Langmuir	q_m = 179.332 K_L = 0.251	0.9068	18.78	15.57	551.36

Units: *T, °C; K_F, (mg/g)(L/mg)$^{(1/n_F)}$; n_F, dimensionless; q_m, mg/g; K_L, L/mg; R^2, dimensionless; RMSE, mg/g; MAE, mg/g; χ^2, mg/g.*

Table 4. Unweighted nonlinear Freundlich, Langmuir, and Redlich–Peterson isotherm parameters and statistical fitting criteria for MO adsorption onto HSCA at different temperatures

T	Model	Parameters ± SE	R^2	RMSE	MAE	χ^2	AICc	BIC
10.0	Freundlich	K_F = 15.049 ± 0.492 n_F = 2.236 ± 0.036	0.9988	1.61	1.15	0.40	17.51	17.44
	Langmuir	q_m = 165.600 ± 12.793 K_L = 0.028 ± 0.006	0.9664	8.62	7.91	165.96	61.22	61.15
	Redlich–Peterson	K_{RP} = 1.00 × 10^8 ± 1.71 × 10^6 a_{RP} = 6.65 × 10^6 ± 1.14 × 10^5 β = 0.553 ± 0.008	0.9988	1.61	1.10	0.40	20.97	20.00
20.0	Freundlich	K_F = 23.940 ± 0.748 n_F = 2.593 ± 0.049	0.9985	2.03	1.37	0.57	23.65	23.57
	Langmuir	q_m = 167.032 ± 12.700 K_L = 0.051 ± 0.014	0.9522	11.50	10.515	446.55	68.70	68.63
	Redlich–Peterson	K_{RP} = 1.00 × 10^8 ± 1.64 × 10^6 a_{RP} = 4.18 × 10^6 ± 6.84 × 10^4 β = 0.614 ± 0.008	0.9985	2.03	1.37	0.57	27.11	26.14
30.4	Freundlich	K_F = 38.458 ± 0.690 n_F = 3.193 ± 0.045	0.9992	1.665	1.34	2.13	18.29	18.22
	Langmuir	q_m = 163.058 ± 10.588 K_L = 0.1325 ± 0.0384	0.9424	13.80	12.27	726.06	73.43	73.36
	Redlich–Peterson	K_{RP} = 2845 ± 1626 a_{RP} = 72.34 ± 42.06 β = 0.692 ± 0.004	0.9995	1.33	1.13	0.81	16.12	15.15
40.0	Freundlich	K_F = 46.090 ± 0.894 n_F = 3.371 ± 0.056	0.9988	2.09	1.54	4.31	24.30	24.32
	Langmuir	q_m = 169.683 ± 11.631 K_L = 0.194 ± 0.064	0.9316	16.09	14.26	791.51	77.43	77.36
	Redlich–Peterson	K_{RP} = 2910 ± 1000 a_{RP} = 60.94 ± 21.45 β = 0.712 ± 0.004	0.9996	1.26	1.08	1.25	14.67	13.69

Units: *T, °C; K_F, (mg/g)(L/mg)$^{(1/nF)}$; n_F, dimensionless; q_m, mg/g; K_L, L/mg; K_{RP}, L/g; a_{RP}, (L/mg)$^{\beta}$; β, dimensionless; R^2, dimensionless; RMSE, mg/g; MAE, mg/g; χ^2, mg/g; AICc and BIC, dimensionless.*

temperatures. At 10.0 °C, the linearized Freundlich model yielded KF = 15.217, nF = 2.247, R2 = 0.9988, and RMSE = 1.61 mg/g, whereas Langmuir gave R2 = 0.9315 and RMSE = 12.31 mg/g. A similar difference was observed at 20.0 °C, where Freundlich produced R^2 =

0.9985 and RMSE = 2.06 mg/g compared with R^2 = 0.9168 and RMSE = 15.18 mg/g for Langmuir. At the two higher temperatures, the deviation associated with linearization became more pronounced. The Freundlich R^2 decreased to 0.9897 and 0.9783 at 30.4 and 40.0 °C, respectively, while the corresponding RMSE values increased to 5.82 and 9.06 mg/g. These results indicate that transformation of the original equilibrium data affected the fitting quality, particularly at higher temperatures. Accordingly, the nonlinear analyses were given greater emphasis because nonlinear regression preserves the original response scale and avoids distortions of the error structure introduced by linearization [43–47].

The unweighted nonlinear results summarized in Table 4 demonstrated that the relative statistical performance of the models varied with temperature. At 10.0 °C, Freundlich yielded K_F = 15.049 ± 0.492 and n_F = 2.236 ± 0.036, with R^2 = 0.9988, RMSE = 1.61 mg/g, AICc = 17.51, and BIC = 17.44. Although Redlich–Peterson produced essentially the same R^2 and RMSE, its fitted constants became extremely large, with K_{RP} = 1.00 × 10^8 ± 1.71 × 10^6 L/g and a_{RP} = 6.65 × 10^6 ± 1.14 × 10^5 (L/mg)$^{\beta}$. A similar pattern was observed at 20.0 °C: Freundlich yielded K_F = 23.940 ± 0.748 and n_F = 2.593 ± 0.049, with R^2 = 0.9985, RMSE = 2.03 mg/g, AICc = 23.65, and BIC = 23.57, whereas the Redlich–Peterson constants again reached very large values despite providing similar goodness-of-fit statistics. The much smaller number of parameters and the lower information-criterion values therefore favored Freundlich at the two lower temperatures. The very large Redlich–Peterson constants at 10 and 20.0 °C also indicate substantial parameter correlation and limited independent interpretability of K_{RP} and a_{RP} under these conditions.

At 30.4 °C, however, the Redlich–Peterson model provided the strongest unweighted nonlinear description. It yielded K_{RP} = 2845 ± 1626 L/g, a_{RP} = 72.34 ± 42.06 (L/mg)$^{\beta}$, and β = 0.692 ± 0.004, together with R^2 = 0.9995, RMSE = 1.33 mg/g, AICc = 16.12, and BIC = 15.15. The corresponding Freundlich fit remained satisfactory, with K_F = 38.458 ± 0.690, n_F = 3.193 ± 0.045, R^2 = 0.9992, RMSE = 1.665 mg/g, and AICc = 18.29. At 40.0 °C, Redlich–Peterson again provided the lowest unweighted fitting error and information criteria, yielding K_{RP} = 2910 ± 1000 L/g, a_{RP} = 60.94 ± 21.45 (L/mg)$^{\beta}$, β = 0.712 ± 0.004, R^2 = 0.9996, RMSE = 1.26 mg/g, and AICc = 14.67. Freundlich remained highly satisfactory at this temperature but produced a somewhat larger RMSE of

2.09 mg/g and AICc of 24.30. Thus, no single unweighted nonlinear model was statistically superior over the entire investigated temperature range: Freundlich was favored at 10.0 and 20.0 °C, whereas Redlich–Peterson provided the strongest statistical description at 30.4 and 40.0 °C.

In contrast, the Langmuir model consistently provided poorer agreement with the experimental equilibrium data. In the unweighted nonlinear analysis, its R^2 values ranged from 0.9316 to 0.9664, while RMSE ranged from 8.62 to 16.09 mg/g. The fitted Langmuir q_m values were approximately 163–170 mg/g, substantially exceeding the experimentally observed adsorption capacities within the investigated concentration range. Because the experimental equilibrium profiles did not exhibit a clear saturation plateau, these q_m values should be considered model-based extrapolations rather than experimentally established maximum adsorption capacities. This limitation also illustrates why a numerically estimated saturation capacity should not be interpreted independently of the experimental concentration range and the observed shape of the equilibrium curve [45,46].

The weighted nonlinear analysis presented in Table 5 provided a complementary assessment by incorporating the experimental uncertainty of the equilibrium measurements. Freundlich remained highly competitive across all temperatures. At 10.0 °C, the weighted Freundlich fit yielded K_F = 15.210 ± 0.092 and n_F = 2.239 ± 0.009, with R^2 = 0.9987, RMSE = 1.72 mg/g, and AICc = 35.15, compared with an AICc of 38.56 for Redlich–Peterson. At 20.0 °C, Freundlich again provided the lower AICc (36.46 versus 39.17 for Redlich–Peterson). At 30.4 °C, Freundlich yielded K_F = 36.867 ± 0.241 and n_F = 3.080 ± 0.020, with R^2 = 0.9986, RMSE = 2.13 mg/g, and AICc = 52.14, while Redlich–Peterson gave AICc = 53.58. At 40.0 °C, the two models became statistically very close: Redlich–Peterson yielded AICc = 56.15 compared with 56.37 for Freundlich. The dependence of model ranking on the adopted error structure, particularly at the higher temperatures, indicates that the unweighted preference for Redlich–Peterson should not be interpreted as evidence that this model uniquely represents the physical adsorption process. Instead, Freundlich and Redlich–Peterson should be regarded as competing empirical descriptions of the equilibrium behavior.

The Freundlich parameters exhibited a systematic temperature dependence. For the unweighted nonlinear fits, K_F increased from 15.049 ± 0.492 at 10.0 °C to 23.940 ± 0.748 at 20.0 °C, 38.458 ± 0.690 at 30.4 °C, and 46.090 ± 0.894 at 40.0 °C. A comparable trend was obtained from the weighted nonlinear analysis, where K_F increased from 15.210 ± 0.092 to 45.078 ± 0.410 over the same temperature range. The increase in K_F is consistent with the experimentally observed enhancement of MO

Table 5. Weighted nonlinear Freundlich, Langmuir, and Redlich–Peterson isotherm parameters and fitting statistics for MO adsorption onto HSCA at different temperatures.

T	Model	Parameters ± SE	R^2	RMSE	MAE	χ^2	AICc	BIC
10.0	Freundlich	K_F = 15.210 ± 0.092 n_F = 2.239 ± 0.009	0.9987	1.72	1.04	0.43	35.15	35.08
	Langmuir	q_m = 132.279 ± 20.456 K_L = 0.045 ± 0.013	0.9364	11.86	8.67	120.66	4.60×10^4	4.60×10^4
	Redlich–Peterson	K_{RP} = 6122 ± 14806 a_{RP} = 400.65 ± 973.40 β = 0.555 ± 0.003	0.9987	1.70	1.024	0.42	38.56	37.59
20.0	Freundlich	K_F = 24.100 ± 0.097 n_F = 2.585 ± 0.007	0.9981	2.28	1.44	0.67	36.46	36.39
	Langmuir	q_m = 97.630 ± 20.696 K_L = 0.184 ± 0.076	0.7241	27.64	18.00	271.89	3.19×10^5	3.19×10^5
	Redlich–Peterson	K_{RP} = 18395 ± 15313 a_{RP} = 756.92 ± 635.38 β = 0.616 ± 0.003	0.9983	2.15	1.33	0.59	39.17	38.19
30.4	Freundlich	K_F = 36.867 ± 0.241 n_F = 3.080 ± 0.020	0.9986	2.13	1.62	1.96	52.14	52.07
	Langmuir	q_m = 122.524 ± 8.294 K_L = 0.3081 ± 0.0373	0.8557	21.84	15.71	410.93	1.39×10^5	1.39×10^5
	Redlich–Peterson	K_{RP} = 20090 ± 13252 a_{RP} = 538.24 ± 359.24 β = 0.680 ± 0.004	0.9990	1.815	1.27	1.64	53.58	52.61
40.0	Freundlich	K_F = 45.078 ± 0.410 n_F = 3.310 ± 0.028	0.9987	2.21	1.57	3.97	56.37	56.30
	Langmuir	q_m = 127.273 ± 8.293 K_L = 0.366 ± 0.120	0.8336	25.10	18.60	567.07	2.21×10^4	2.21×10^4
	Redlich–Peterson	K_{RP} = 8564 ± 4466 a_{RP} = 185.61 ± 98.87 β = 0.704 ± 0.004	0.9993	1.68	1.23	2.45	56.15	55.18

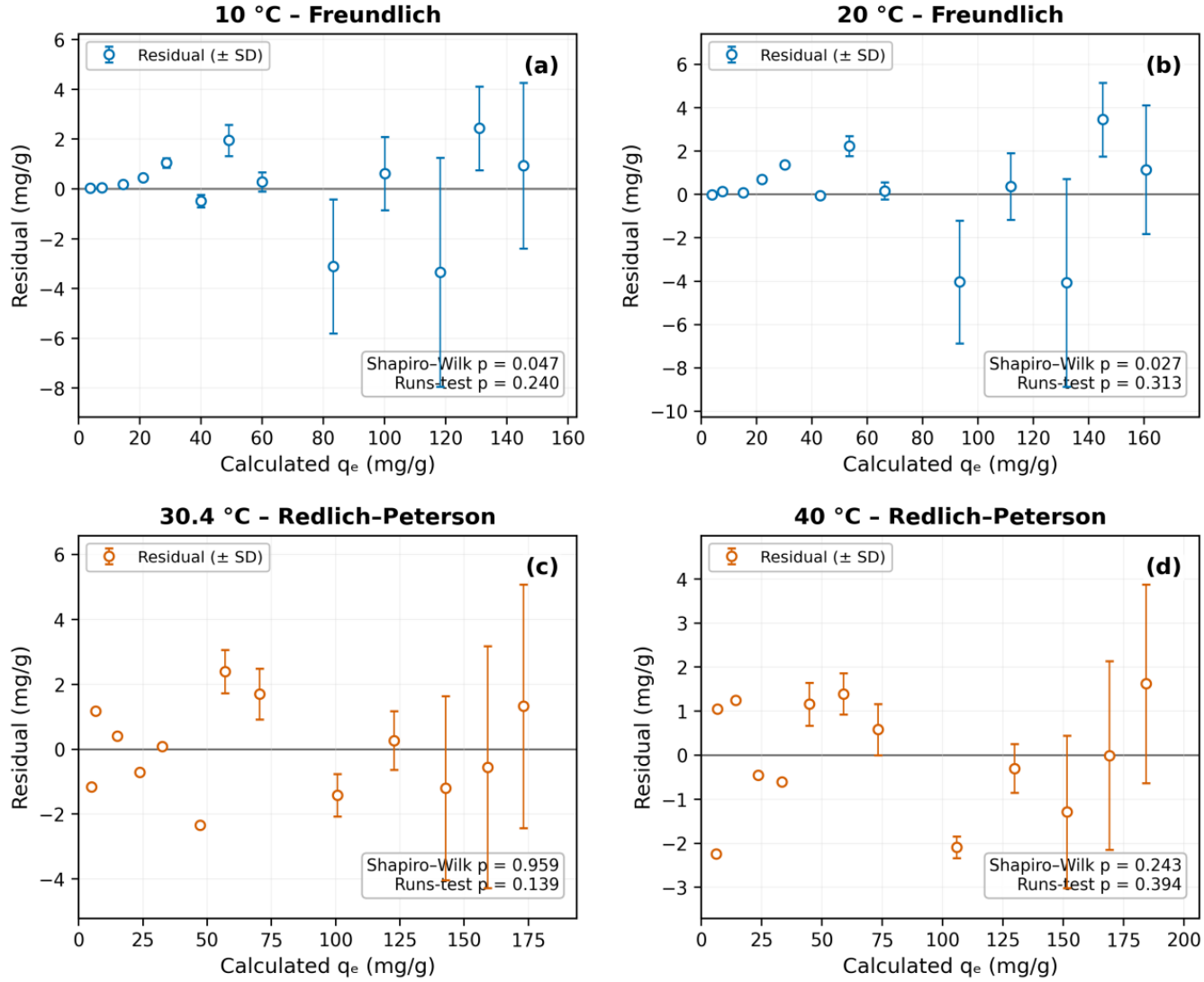


Figure 6. Residual plots of the selected unweighted nonlinear isotherm models at different temperatures.

uptake with increasing temperature and with the endothermic tendency discussed in Section 3.3. Similar temperature-dependent MO adsorption behavior has been reported for mesoporous carbon materials [47]. Nevertheless, K_F is an empirical parameter whose estimated magnitude can depend on the temperature, concentration range, data distribution, and adopted fitting approach; therefore, its increase should not be interpreted independently as direct evidence of an increase in intrinsic adsorption affinity.

The Freundlich intensity parameter n_F remained greater than unity throughout the investigated temperature range. For the unweighted nonlinear analysis, n_F increased from 2.236 ± 0.036 at 10.0 °C to 3.371 ± 0.056 at 40.0 °C, while the weighted nonlinear approach produced comparable values of 2.239 ± 0.009 and 3.310 ± 0.028, respectively. Values of $n_F > 1$ are generally associated with favorable adsorption within the empirical Freundlich framework [45,46]. However, the temperature-dependent increase in n_F is interpreted here as a change in the fitted adsorption-intensity parameter rather than as independent evidence of progressively stronger adsorption favorability.

Residual analysis provided an additional assessment of model adequacy. As shown in Fig. 6, the Wald–Wolfowitz runs-test results were not significant for the selected unweighted nonlinear models at any investigated temperature, indicating no strong evidence of systematic ordering in the residual sequence. The Shapiro–Wilk test indicated residual distributions consistent with normality at 30.4 and 40.0 °C, with p-values of 0.959 and 0.796, respectively. In contrast, the corresponding p-values at 10.0 and 20.0 °C were 0.047 and 0.027, indicating some departure from normality despite the high R^2 values. Given the relatively small number of equilibrium observations, these residual diagnostics were interpreted together with the graphical residual patterns, fitting errors, parameter uncertainties, and information criteria rather than as stand-alone criteria for model adequacy.

Overall, the equilibrium results are more consistent with non-ideal and heterogeneous adsorption behavior than with the idealized homogeneous monolayer

description represented by the Langmuir model. The consistently satisfactory Freundlich description and the

3.3. Apparent thermodynamic analysis

Table 6. Comparison of the methyl orange adsorption performance of HSCA with selected biomass-derived biochars and activated carbons reported in the literature.

Adsorbent	Biomass precursor / preparation	Experimental conditions	Capacity type	Adsorption capacity (mg/g)	Best-fit isotherm	Ref.
AC	Wood sawdust-derived activated carbon	pH 3.0; 20.0 °C; C_0 = 10–200 mg/L; 45 min	Langmuir q_{max}	42.51	Langmuir	[5]
PJW biochar	*Prosopis juliflora* waste-derived biochar	pH 6.0; 25.0 °C; C_0 = 20–150 mg/L; 150 rpm	Langmuir q_{max}[a]	8.08	Temkin	[6]
RHB	Rice husk-derived biochar	pH ≈ 3; 25 ± 2 °C; C_0 = 10–200 mg/L; 240 min	Langmuir q_{max}	31.63	Langmuir	[9]
BC	Poultry manure-derived biochar	pH 4.0; 23 ± 2 °C; C_0 = 0–200 mg/L; 1440 min; 150 rpm	Langmuir q_{max}	98.23	Langmuir	[10]
PAC	H_3PO_4-activated spent-coffee-ground activated carbon	pH 3.0; 24.0 °C; C_0 = 5–40 mg/L; 120 min; 350 rpm	Langmuir q_{max}[b]	333.33	Freundlich	[11]
HSCA	Hazelnut shell-based carbonaceous adsorbent	pH 3.0; 30.4 °C; C_0 = 42.65 mg/L; 360 min; 225 rpm	Experimental q_e	32.183±0.086	Redlich–Peterson[c]	This study

[a] Langmuir-derived q_{max}; Temkin provided the best fit to the equilibrium data.
[b] Although Freundlich provided the better equilibrium fit, 333.33 mg/g corresponds to the Langmuir-derived q_{max}
[c] Redlich–Peterson provided the lowest AICc in the unweighted nonlinear comparison at 30.4 °C.

competitive Redlich–Peterson fits at the higher temperatures are compatible with the presence of structurally and energetically non-uniform adsorption environments within HSCA. This interpretation is also consistent with the independent physicochemical and molecular-level results presented in the subsequent sections, including the micro–mesoporous pore structure, oxygen-containing surface functionalities, disordered aromatic carbon domains, and multiple local MO–surface interactions. Nevertheless, isotherm models provide empirical descriptions of equilibrium behavior and should not be interpreted as direct or exclusive proof of a particular adsorption mechanism [45–47].

To place the adsorption performance of HSCA in the context of previously reported biomass-derived carbonaceous adsorbents, the present results are compared with selected literature data in Table 6. The experimentally observed adsorption capacity of HSCA under the kinetic reference conditions was 32.183 ± 0.086 mg/g at C_0 = 42.65 mg/L, pH 3.0, 30.4 °C, and 225 rpm. This value falls within the range reported for the selected biomass-derived biochars and activated carbons and is numerically comparable to that reported for rice-husk-derived biochar. However, direct numerical comparisons should be made cautiously because the literature values were obtained under different experimental conditions, including different pH values, initial concentrations, temperatures, contact times, adsorbent preparation procedures, and adsorbent dosages. In addition, some reported capacities represent Langmuir-derived q_{max} values rather than directly measured equilibrium capacities. Therefore, Table 6 should be regarded as a contextual performance comparison rather than as a strictly equivalent ranking of adsorption capacities.

The apparent thermodynamic behavior of MO adsorption onto HSCA was evaluated to assess the effects of temperature and initial concentration on the adsorption process. The corresponding ln K_c versus 1000/T plots and residual distributions are presented in Fig. 7, while the apparent thermodynamic parameters and statistical fit criteria are summarized in Table 7. ΔG_{app} was calculated using the apparent equilibrium constant derived from the concentration ratio $[(C_0-C_e)/C_e]$. The term "apparent" was intentionally used because this concentration-based ratio does not represent a rigorous activity-based standard thermodynamic equilibrium constant. Therefore, the calculated ΔG_{app}, ΔH_{app}, and ΔS_{app} values should be interpreted as conditional thermodynamic indicators for the present adsorption system rather than as absolute standard thermodynamic functions [48–50].

The ΔG_{app} values were negative over the entire concentration and temperature range, suggesting that MO adsorption onto HSCA was favorable within the apparent thermodynamic framework and under the investigated conditions. For each initial concentration, ΔG_{app} became more negative with increasing temperature, suggesting that adsorption was increasingly favored at elevated temperatures. For example, at C_0 = 10 mg/L, ΔG_{app} decreased from −9.02 kJ/mol at 10.0 °C to −19.34 kJ/mol at 40.0 °C, whereas at C_0 = 350 mg/L it changed from −0.42 to −2.08 kJ/mol over the same temperature range. These results suggest that increasing temperature enhanced the apparent thermodynamic driving force of adsorption. In contrast, increasing C_0 shifted ΔG_{app} toward less negative values, indicating a gradual reduction in adsorption driving force as the available high-affinity adsorption sites became progressively occupied. This concentration-

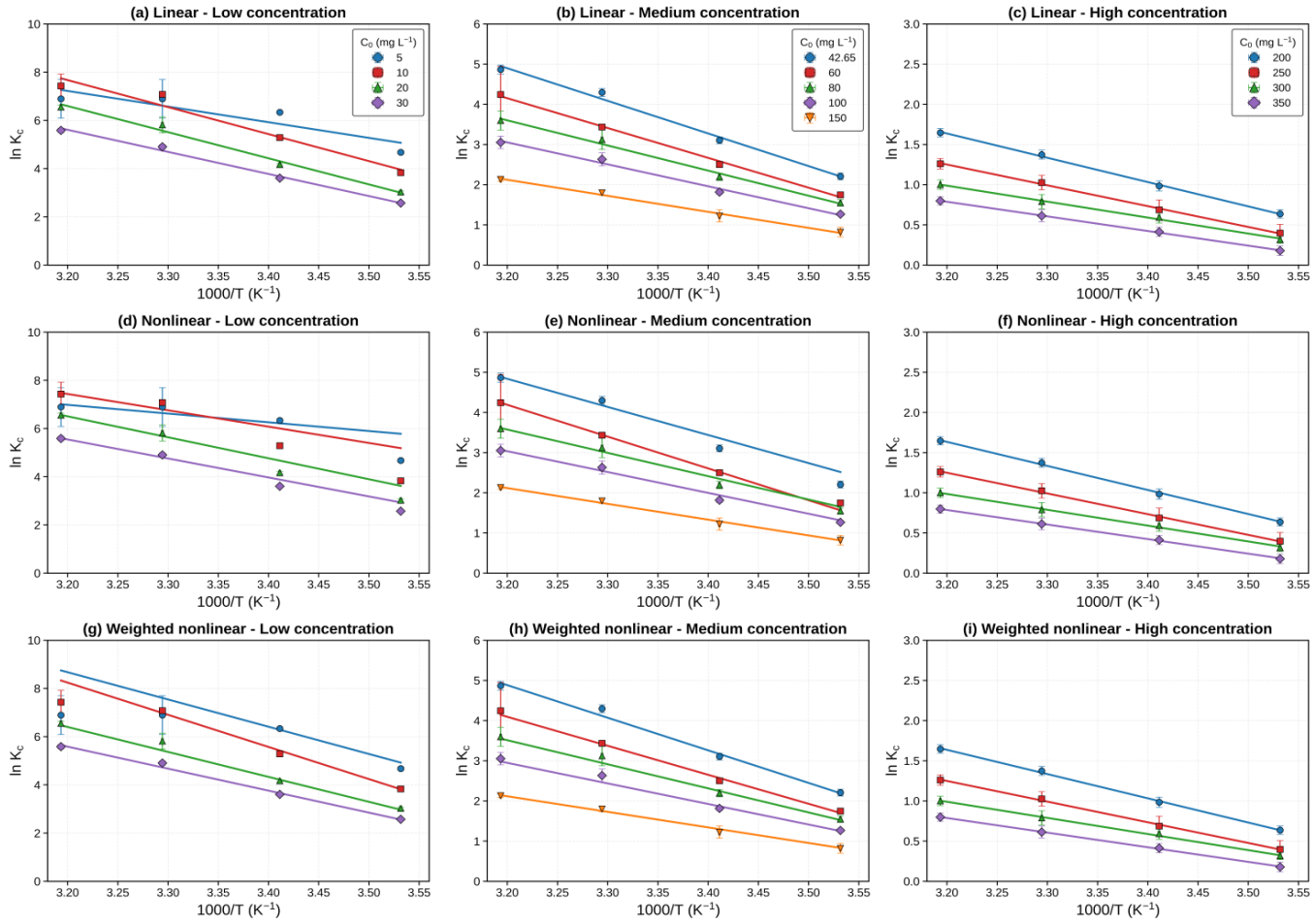


Figure 7. Van't Hoff plots for methyl orange adsorption onto HSCA at different concentration regions using linear, nonlinear, and weighted nonlinear fitting approaches

dependent behavior is consistent with the Freundlich isotherm results, which suggested adsorption on heterogeneous HSCA surface domains with different site affinities.

The concentration level of C_0 = 42.65 mg/L represented an intermediate condition within the investigated thermodynamic dataset and is particularly relevant because it corresponds to the optimized adsorption region. At this concentration, ΔG_{app} was −10.84 kJ/mol at 30.4 °C, supporting the favorable character of MO adsorption under the optimized experimental condition within the apparent thermodynamic framework. In addition, ΔG_{app} decreased from −5.20 to −12.67 kJ/mol as temperature increased from 10.0 to 40.0 °C, further supporting the temperature-enhanced nature of the adsorption process. ΔH_{app} and ΔS_{app} were subsequently estimated using linear, nonlinear, and weighted nonlinear Van't Hoff approaches.

The linear Van't Hoff treatment assumes that ΔH_{app} and ΔS_{app} remain approximately independent of temperature over the investigated range; under this condition, a linear relationship between lnK_c and $1/T$ is expected [51]. The generally satisfactory linearity of the Van't Hoff relationships supports the applicability of this approximation over the investigated temperature interval (10.0–40.0 °C). However, considering the limited number of temperature points, the observed linearity should not be regarded as definitive evidence of strictly temperature-independent ΔH_{app} and ΔS_{app} values. Accordingly, the derived ΔH_{app} and ΔS_{app} values should be interpreted as approximate apparent thermodynamic parameters representative of the investigated temperature range.

Positive ΔH_{app} values were obtained for all fitting approaches, suggesting an endothermic tendency within the investigated concentration range. In the linear Van't Hoff approach, ΔH_{app} decreased from 93.13 kJ/mol at C_0 = 10 mg/L to 15.14 kJ/mol at C_0 = 350 mg/L. A similar concentration-dependent decrease was observed for ΔS_{app}, which declined from 361.80 to 54.98 J/mol K over the same concentration range. This trend suggests that adsorption at lower concentrations preferentially occurred on energetically favorable sites, whereas increasing solute loading promoted adsorption on progressively less energetic sites as surface coverage increased. At C_0 = 42.65 mg/L, the linear and weighted nonlinear Van't Hoff approaches yielded highly

Table 7. Apparent thermodynamic parameters and statistical fit criteria obtained from linear, nonlinear, and weighted nonlinear Van't Hoff approaches for MO adsorption onto HSCA.

	C_0 (mg/L)	ΔH_{app} (kJ/mol)	ΔS_{app} (J/mol K)	ΔG_{app} (kJ mol^{-1}) 10 °C	20 °C	30.4 °C	40 °C	R^2	RMSE	MAE	χ^2
Linear Van't Hoff approach	5	53.94	232.64	-11.00	-15.44	-17.40	-17.95	0.8159	0.390	0.384	0.102
	10	93.13	361.80	-9.02	-12.88	-17.86	-19.34	0.9606	0.287	0.231	0.049
	20	90.13	343.26	-7.11	-10.15	-14.67	-17.05	0.9880	0.151	0.130	0.017
	30	76.16	290.36	-6.05	-8.78	-12.38	-14.54	0.9931	0.097	0.079	0.008
	42.65	67.51	256.75	-5.20	-7.57	-10.84	-12.67	0.9905	0.101	0.083	0.010
	60	61.74	232.10	-4.12	-6.09	-8.66	-11.05	0.9964	0.056	0.051	0.005
	80	52.00	196.34	-3.64	-5.35	-7.88	-9.36	0.9913	0.074	0.066	0.008
	100	45.41	170.69	-2.98	-4.42	-6.64	-7.95	0.9907	0.067	0.060	0.008
	150	33.17	123.79	-1.93	-2.98	-4.54	-5.55	0.9936	0.041	0.036	0.005
	200	25.14	94.05	-1.50	-2.40	-3.47	-4.29	0.9987	0.014	0.012	0.001
	250	21.53	79.31	-0.93	-1.67	-2.59	-3.28	0.9983	0.013	0.012	0.001
	300	16.51	61.03	-0.75	-1.44	-1.99	-2.60	0.9969	0.014	0.012	0.002
	350	15.14	54.98	-0.42	-1.01	-1.55	-2.08	0.9993	0.006	0.005	0.001
Nonlinear Van't Hoff approach	5	30.08	154.30	-11.00	-15.44	-17.40	-17.95	0.6017	0.574	0.398	0.226
	10	56.33	242.05	-9.02	-12.88	-17.86	-19.34	0.7095	0.780	0.601	0.452
	20	72.33	285.54	-7.11	-10.15	-14.67	-17.05	0.9173	0.397	0.311	0.157
	30	65.48	255.65	-6.05	-8.78	-12.38	-14.54	0.9595	0.234	0.189	0.067
	42.65	58.14	226.27	-5.20	-7.57	-10.84	-12.67	0.9588	0.210	0.176	0.061
	60	65.82	245.46	-4.12	-6.09	-8.66	-11.05	0.9903	0.093	0.053	0.022
	80	48.27	184.19	-3.64	-5.35	-7.88	-9.36	0.9831	0.103	0.091	0.019
	100	43.13	163.25	-2.98	-4.42	-6.64	-7.95	0.9867	0.080	0.069	0.013
	150	32.67	122.16	-1.93	-2.98	-4.54	-5.55	0.9933	0.042	0.033	0.005
	200	24.88	93.20	-1.50	-2.40	-3.47	-4.29	0.9986	0.015	0.013	0.001
	250	21.43	78.96	-0.93	-1.67	-2.59	-3.28	0.9983	0.014	0.011	0.001
	300	16.38	60.61	-0.75	-1.44	-1.99	-2.60	0.9968	0.014	0.012	0.002
	350	15.06	54.72	-0.42	-1.01	-1.55	-2.08	0.9993	0.006	0.005	0.001
Weighted nonlinear Van't Hoff approach	5	94.02	372.96	-11.00	-15.44	-17.40	-17.95	0.5130	1.002	0.717	0.473
	10	110.90	423.41	-9.02	-12.88	-17.86	-19.34	0.8997	0.458	0.287	0.102
	20	86.05	328.57	-7.11	-10.15	-14.67	-17.05	0.9787	0.201	0.143	0.030
	30	75.86	289.19	-6.05	-8.78	-12.38	-14.54	0.9928	0.099	0.077	0.008
	42.65	67.44	256.39	-5.20	-7.57	-10.84	-12.67	0.9903	0.102	0.082	0.010
	60	60.01	226.07	-4.12	-6.09	-8.66	-11.05	0.9950	0.067	0.060	0.006
	80	49.83	188.67	-3.64	-5.35	-7.88	-9.36	0.9859	0.095	0.074	0.012
	100	42.54	160.63	-2.98	-4.42	-6.64	-7.95	0.9815	0.094	0.076	0.015
	150	32.23	120.73	-1.93	-2.98	-4.54	-5.55	0.9922	0.045	0.036	0.006
	200	25.08	93.85	-1.50	-2.40	-3.47	-4.29	0.9987	0.014	0.012	0.001
	250	21.38	78.81	-0.93	-1.67	-2.59	-3.28	0.9983	0.014	0.011	0.001
	300	16.69	61.64	-0.75	-1.44	-1.99	-2.60	0.9967	0.014	0.012	0.001
	350	15.13	54.96	-0.42	-1.01	-1.55	-2.08	0.9993	0.006	0.005	0.001

consistent apparent thermodynamic parameters, with ΔH_{app} values of 67.51 and 67.44 kJ/mol and ΔS_{app} values of 256.75 and 256.39 J/mol K, respectively. The positive ΔS_{app} values may reflect increased disorder at the solid–liquid interface, possibly associated with the release of structured water molecules from the HSCA surface and the hydration shell of MO during adsorption. Similar endothermic and entropy-favored behavior has been reported for MO adsorption onto mesoporous carbon materials [46]. Overall, within the limitations of the concentration-based apparent thermodynamic framework, the results suggest that MO adsorption onto HSCA exhibited favorable, endothermic, and concentration-dependent tendencies under the investigated conditions, with temperature apparently promoting adsorption and increasing initial concentration gradually reducing the apparent thermodynamic driving force.

3.4. Molecular-level investigation of MO adsorption onto HSCA using density functional theory

To establish a molecular-level understanding of the adsorption mechanism, the experimental surface charge characteristics of HSCA were interpreted together with the DFT results obtained for protonated MO, the HSCA surface model, and the optimized MO-HSCA adsorption complex. The pH-drift and pH-dependent zeta-potential profiles of HSCA are presented in Fig. 8. Surface

characterization revealed a pH_{PZC} value of 6.39 and a pH_{IEP} value of 4.12.

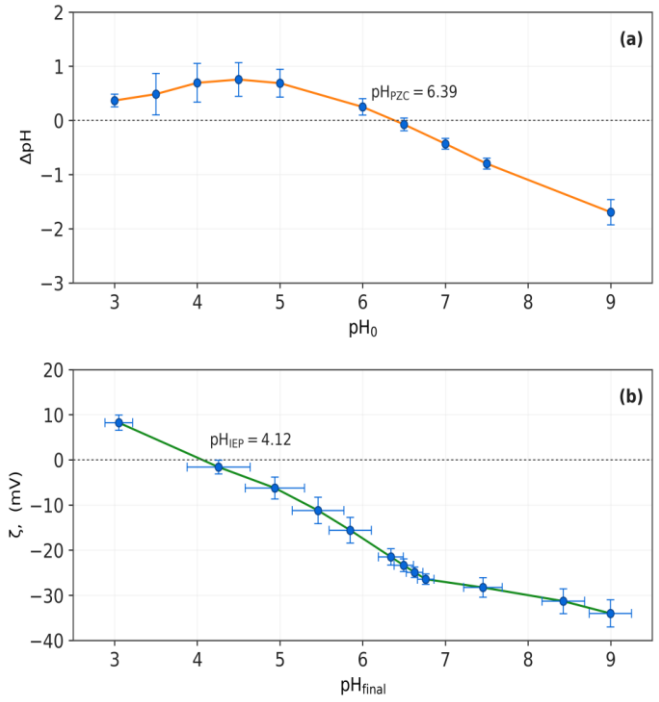


Figure 8. Surface charge characteristics of HSCA: (a) pH_{PZC} determined by the pH-drift method and (b) pH_{IEP} determined from the pH-dependent zeta-potential profile.

Although both parameters characterize the surface charge behavior, they represent different interfacial properties and therefore are not necessarily identical. The pH_{PZC} determined by the pH drift method is associated with the condition of zero net surface charge, whereas the pH_{IEP} obtained from zeta potential measurements corresponds to the pH at which the electrokinetic potential at the shear plane becomes zero. For porous carbonaceous materials, differences between pH_{PZC} and pH_{IEP} have been reported and may be associated with surface heterogeneity, the distribution of surface functional groups between internal and external surfaces, and ion–surface interactions at the solid–liquid interface [52,53]. Importantly, the experimental adsorption pH (pH 3.0) was below both pH_{PZC} and pH_{IEP}, indicating a positive net surface charge and a positive electrokinetic potential under the experimental adsorption conditions.

Since MO retains its sulfonate functionality in acidic media, favorable electrostatic attraction between negatively polarized sulfonate oxygen atoms and positively charged surface sites can be expected. This interpretation is consistent with the established role of solution pH and point of zero charge in controlling electrostatic interactions at carbonaceous adsorbent-solution interfaces [54,55]. However, the experimental adsorption behavior cannot be explained solely by electrostatic attraction. Therefore, the surface charge results suggest that electrostatic attraction facilitates the initial approach of MO toward HSCA under acidic conditions, while the final adsorbed state is further stabilized by additional molecular interactions. Although adsorption experiments were performed only at pH 3.0, solution pH may influence MO uptake through changes in the interfacial charge characteristics of HSCA. As the pH increases above the pH_{IEP} (4.12), the zeta potential becomes negative, which may progressively reduce favorable electrostatic interactions with anionic MO and introduce electrostatic repulsion. Above the pH_{PZC} (6.39), the net surface charge also becomes negative, which may further favor electrostatic repulsion between HSCA and anionic MO. However, because adsorption experiments were not conducted over a broader pH range, the resulting effect on the overall adsorption capacity cannot be established from the present data. In this context, the finite HSCA cluster used in the DFT calculations should be considered as a local model of an oxygen-functionalized aromatic adsorption domain rather than a complete representation of the heterogeneous carbonaceous material.

The optimized adsorption geometry shown in Fig. 9 revealed that protonated MO adopted an approximately parallel orientation relative to the aromatic HSCA surface. This configuration favors contact between the π-electron system of MO and the graphitic domain of HSCA, thereby supporting extended π-related and dispersion-driven interactions. Such an arrangement is chemically reasonable because adsorption of aromatic organic molecules on carbon surfaces is commonly governed by a combination of π–π interactions, dispersion forces, hydrophobic effects, and interactions with oxygen-containing surface functionalities [55,56]. In addition to the parallel orientation, the optimized complex showed a localized O–H···O contact between an oxygen-containing HSCA surface group and the sulfonate moiety of MO, indicating that adsorption is assisted by both extended surface interactions and localized hydrogen bonding. The optimized complex was confirmed as a true energy minimum by the absence of imaginary frequencies, supporting the stability of the proposed adsorption configuration.

The calculated adsorption energy of −179.8 kJ/mol, together with ΔH_{ads} and ΔG_{ads} values of −213.9 and −136.2 kJ/mol, respectively, indicates that complex formation is energetically favorable within the employed computational model. However, these values should be interpreted as model-dependent molecular-level stabilization energies rather than direct macroscopic adsorption enthalpies, since cluster size, protonation state, solvation treatment, dispersion correction, and basis-set effects can influence calculated adsorption energies [57,58]. In addition, because BSSE correction

was not applied, the magnitude of the calculated adsorption energy may be somewhat overestimated; therefore, the reported value should be interpreted within the limitations of the adopted basis set and computational protocol. In particular, the finite HSCA cluster represents a selected oxygen-functionalized aromatic adsorption domain rather than the complete heterogeneous carbon surface, and the calculated adsorption energy is therefore specific to this local model. The protonation state adopted for MO under the acidic experimental conditions affects its charge distribution and consequently the electrostatic and hydrogen-bonding contributions to complex stabilization. Moreover, the GD3BJ dispersion correction accounts for dispersion interactions over the extended aromatic contact region in the approximately parallel MO–HSCA configuration, and the treatment of such dispersion contributions can substantially influence calculated adsorption energies [59]. Comparably large adsorption or interaction energies have also been reported for MO on graphene oxide and graphene-like carbon models [60,61], indicating that strong overall stabilization can arise from multiple non-covalent contributions in such systems. In particular, Cheng et al. (2023) reported an interaction energy of −37.05 kcal/mol for MO on an N-doped graphene model and attributed the stabilization to the combined contributions of π–π stacking, electrostatic interactions, and hydrogen bonding [61]. Therefore, the magnitude of the calculated adsorption energy should not be interpreted independently as evidence for a specific physical or chemical adsorption mechanism. The negative entropy change of −260.8 J/mol K is consistent with the formation of a more ordered adsorbate–surface assembly after MO binding. This DFT-derived entropy change should not be directly compared with the positive apparent entropy change obtained from the experimental Van't Hoff analysis, because the former refers to an isolated model adsorption complex, whereas the latter reflects the overall solid–liquid interfacial process, including desolvation and water-release contributions.

Frontier molecular orbital (FMO) and molecular electrostatic potential (MEP) analyses provided further evidence for electronic reorganization upon adsorption. The highest occupied molecular orbital (HOMO) and lowest unoccupied molecular orbital (LUMO) energies of protonated MO were −6.10 and −3.39 eV, respectively, corresponding to an energy gap of 2.71 eV. The HSCA surface model showed a gap of 2.30 eV, whereas the MO-HSCA complex displayed a reduced gap of 1.83 eV. This decrease indicates increased polarizability and enhanced interfacial electronic communication after complex

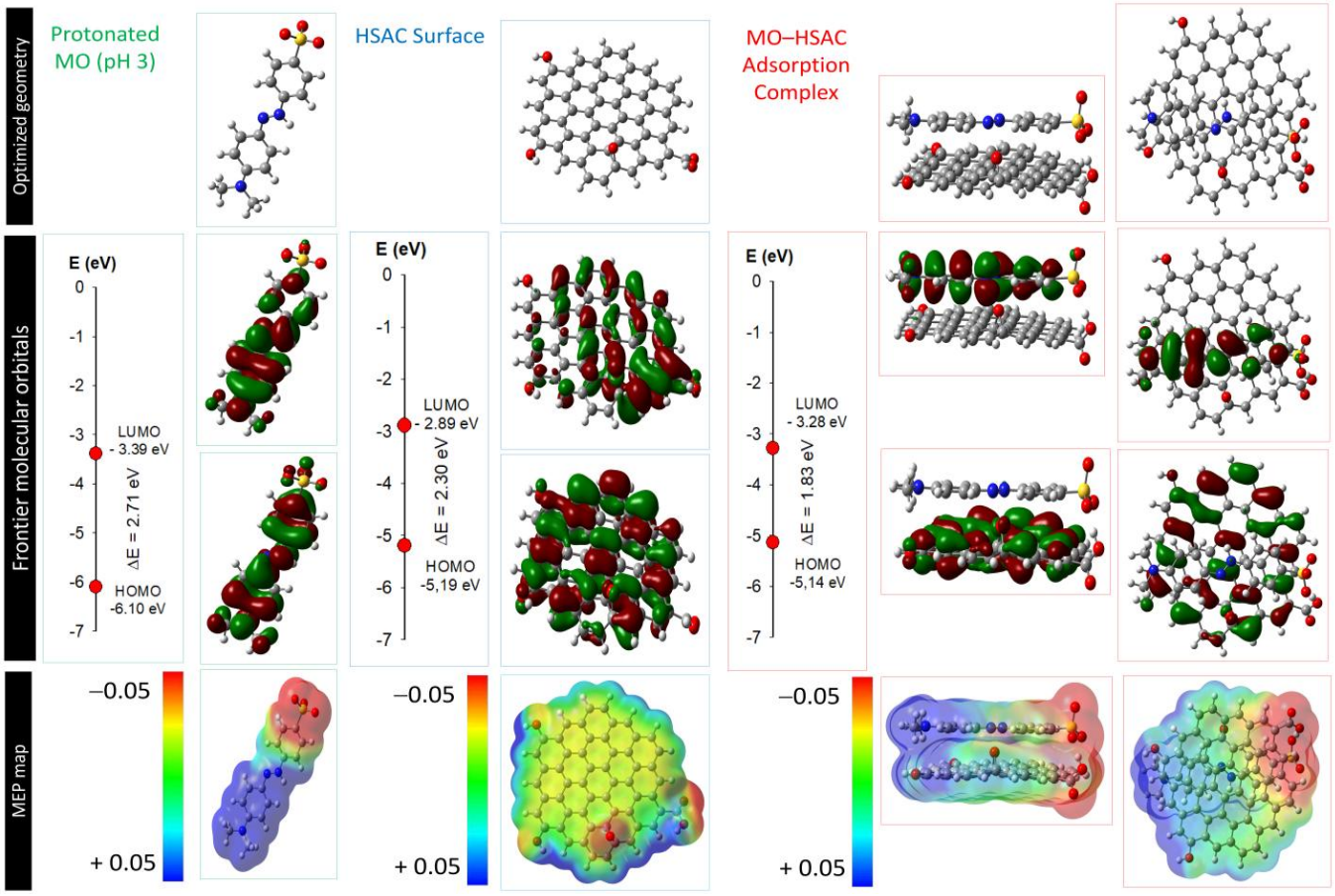


Figure 9. Optimized geometries, frontier molecular orbital (FMO) distributions, highest occupied molecular orbital-lowest unoccupied molecular orbital (HOMO-LUMO) energy gaps, and molecular electrostatic potential (MEP) maps of MO, HSCA, and the MO-HSCA complex

formation. The increase in dipole moment from 51.70 D for isolated MO to 60.87 D for the adsorption complex further supports the formation of a highly polarized interfacial structure. The MEP maps showed that the most electron-rich region of MO was localized around the sulfonate oxygen atoms, while the HSCA model exhibited a heterogeneous electrostatic distribution due to oxygen-containing surface functionalities. After adsorption, redistribution of electrostatic potential across the interface confirmed electrostatic complementarity between the sulfonate moiety of MO and positively polarized HSCA sites. MEP analysis is widely used to identify electron-rich and electron-deficient regions involved in electrostatic attraction and hydrogen bonding; therefore, these results support the experimentally observed preference for MO adsorption under acidic conditions [62].

Hydrogen-bonding geometry and NBO analysis confirmed that localized donor–acceptor interactions contributed to the stabilization of the MO–HSCA complex. A distinct O–H···O hydrogen bond was identified between the surface hydroxyl proton of HSCA and a sulfonate oxygen atom of MO, with an O(99) ···H(61) distance of 1.54 Å and an O(3)–H(61) ···O(99) angle of approximately 167°, indicating a strong directional hydrogen-bonding interaction. Weaker C–H···O contacts were also observed, including C(81)–H(106) ···O(17), C(91)–H(111) ···O(59), and C(86)–H(109) ···O(59), with H···O distances of approximately 2.52, 2.62, and 2.94 Å and angles of about 161°, 144°, and 133°, respectively. The NBO results showed stabilizing donor–acceptor interactions from the lone-pair orbitals of O(99) toward LP*(H61), with E(2) values of 15.69, 0.41, and 63.10 kcal/mol for LP(1), LP(2), and LP(3) O(99) → LP*(H61), respectively. These E(2) values should be interpreted as donor–acceptor stabilization indicators rather than direct experimental bond energies [63].

Complementarily, the NCI analysis shown in Fig. 10 revealed extended green RDG isosurfaces between the aromatic framework of MO and the graphitic HSCA surface, indicating weak attractive interactions associated with dispersion and π–π stacking. The observed intermolecular separations of approximately 3.11–3.62 Å are compatible with aromatic stacking contacts. The NCI/RDG approach is designed to visualize non-covalent interactions from electron-density features and is therefore appropriate for distinguishing localized hydrogen bonding from more spatially extended dispersion interactions [64].

The heterogeneous adsorption behavior inferred from the Freundlich analysis should be distinguished from the local information provided by the DFT model. The finite HSCA cluster represents a single oxygen-functionalized aromatic adsorption domain and therefore does not directly reproduce the distribution of adsorption-site energies implied by the Freundlich isotherm. Nevertheless, the coexistence of electrostatic, π–π, dispersion, and hydrogen-bonding contributions within this representative local domain provides molecular-level context for the non-uniform adsorbate–surface interactions that are consistent with the heterogeneous adsorption behavior described by the Freundlich model. Taken together, the experimental surface charge measurements and DFT results support a cooperative adsorption scenario involving multiple non-covalent interactions, consistent with the kinetic, equilibrium, and apparent thermodynamic trends observed experimentally.

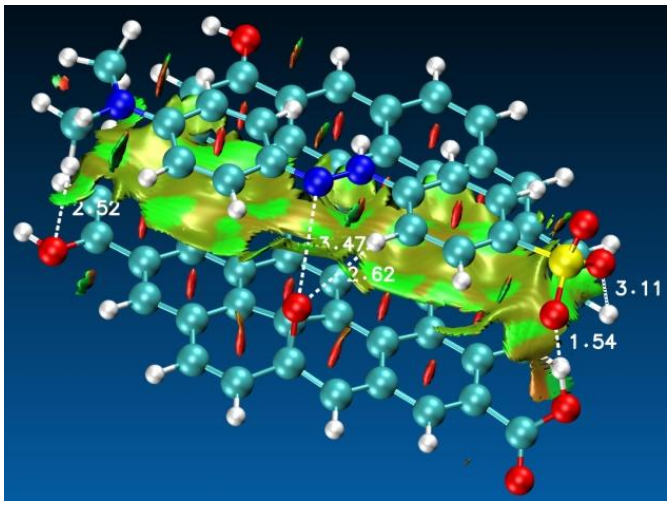


Figure 10. Non-covalent interactions in the MO–HSCA adsorption complex.

3.5. Textural, structural, and morphological characterization of MO adsorption onto HSCA

As shown in Table 8, MO adsorption substantially reduced the N_2-accessible surface area and pore volume of HSCA. The BET surface area decreased from 812.4 to 515.8 m^2/g, corresponding to a reduction of approximately 36.5%. Similarly, the N_2 uptake at the highest measured relative pressure decreased from 505.7 to 320.4 cm^3 STP/g. The micropore surface area decreased from 262.1 to 142.0 m^2/g, while the external surface area decreased from 550.4 to 373.8 m^2/g. The micropore volume exhibited a comparatively greater reduction of 45.8%, decreasing from 0.120 to 0.065 cm^3/g. The BJH cumulative desorption pore volume and NLDFT cumulative pore volume both decreased by approximately 36.5%, from 0.641 to 0.407 cm^3/g and from 0.775 to 0.492 cm^3/g, respectively.

Dye adsorption on porous carbon materials is influenced by pore accessibility, pore connectivity, and molecular dimensions [47]. In contrast to the reductions in surface area and pore volume, the modal NLDFT pore width increased from 1.273 to 1.564 nm (22.9%), while the modal BJH mesopore diameter increased from 3.402

Table 8. Textural properties of pristine and MO-loaded HSCA determined by N_2 adsorption–desorption analysis at 77.30 K

Property	Method/condition	Pristine HSCA	MO-loaded HSCA
BET surface area (m^2/g)	Multipoint BET	812.4	515.8
N_2 uptake at the highest measured relative pressure (cm^3 STP/g)	$P/P_0 \approx 0.99$	505.7	320.4
Micropore surface area (m^2/g)	*t*-plot	262.1	142.0
External surface area (m^2/g)	*t*-plot	550.4	373.8
Micropore volume (cm^3/g)	*t*-plot	0.120	0.065
BJH cumulative desorption pore volume (cm^3/g)	BJH, desorption branch	0.641	0.407
NLDFT cumulative pore volume (cm^3/g)	NLDFT equilibrium model	0.775	0.492
Modal pore width (nm)	NLDFT	1.273	1.564
Modal mesopore diameter (nm)	BJH, desorption branch	3.402	3.802

to 3.802 nm (11.8%). These apparent increases do not necessarily indicate physical expansion of the pores. Instead, they may result from the preferential filling or blockage of narrower pores, which shifts the remaining N_2-accessible pore-size distribution toward larger pore sizes. Desorption-derived pore-size distributions may also be influenced by pore-blocking and network effects [65], as well as cavitation in interconnected pore structures [66]. The equivalent mean pore diameter calculated from the BET surface area and NLDFT cumulative pore volume remained approximately 3.82 nm for both samples, consistent with the nearly proportional decreases in these two parameters.

Taken together, these textural changes provide further insight into the role of the porous structure in MO adsorption. The high initial surface area and developed micro–mesoporous structure of HSCA provide an extensive accessible interfacial domain for MO uptake; however, the adsorption behavior should not be attributed to surface area alone. The comparatively greater loss of micropore surface area and micropore volume indicates that the narrower pore domains were more strongly affected by MO adsorption. This preferential loss of N_2-accessible microporosity is consistent with partial pore filling and pore-mouth blocking, which may progressively restrict access to internal adsorption domains.

This textural response is consistent with the multistage mass-transfer behavior identified by the Weber–Morris and Boyd analyses in Section 3.1, although it does not independently establish the rate-controlling transport mechanism. In particular, the initially faster uptake may be associated with transport toward readily accessible external surface and larger-pore regions, whereas the subsequent slower stage is compatible with increasing transport resistance as adsorption proceeds and less readily accessible internal pore domains become involved, consistent with the multistage transport behavior reported for heterogeneous porous adsorbent systems [32]. The deviation of the Boyd plot from the origin further indicates that intraparticle diffusion was not the sole rate-controlling step and that film diffusion also contributed to the overall mass-transfer resistance.

The coexistence of micro- and mesoporous domains further demonstrates the textural heterogeneity of HSCA. This textural heterogeneity complements the non-uniform adsorption affinities suggested by the Freundlich analysis, although textural heterogeneity alone does not establish energetic surface heterogeneity, which also depends on differences in surface chemistry and adsorbate–surface interactions. Thus, the BET results, together with the kinetic and equilibrium analyses, indicate that MO adsorption is governed by the combined effects of pore accessibility, multistage mass transfer, and heterogeneous adsorption domains rather than by a single textural parameter.

The FTIR spectra of pristine MO, pristine HSCA, and MO-loaded HSCA are shown in Fig. 11. The spectrum of MO displayed characteristic bands associated with its aromatic azo dye structure and sulfonate functionality. The broad band at 3444 cm^{-1} was attributed mainly to physically adsorbed and/or hydration water in the ionic dye matrix rather than to an intrinsic hydroxyl group of MO. The weak band at 2917 cm^{-1} corresponded to aliphatic C–H stretching vibrations of the dimethylamino group. The bands at 1609 and 1522 cm^{-1} were assigned to aromatic C=C stretching and coupled azo–aromatic skeletal vibrations, respectively, while the bands in the 1202–1008 cm^{-1} region were associated mainly with S–O stretching vibrations of the deprotonated sulfonate group. These assignments are consistent with the characteristic vibrational features reported for methyl orange and related sulfonated azo dyes [67,68].

Pristine HSCA exhibited a broad band at 3414 cm^{-1}, which can be attributed to O–H stretching vibrations of hydrogen-bonded surface hydroxyl groups and physically adsorbed water. The band near 2922 cm^{-1} was associated with residual aliphatic C–H groups, whereas the band at approximately 1567 cm^{-1} was assigned to aromatic C=C vibrations within the polyaromatic carbon framework. The broad absorption around 1115 cm^{-1} indicated the presence of oxygen-containing surface functionalities, particularly C–O groups such as phenolic, alcoholic, and ether-type structures [69,70].

After MO adsorption, the MO-loaded HSCA spectrum showed bands at 3400, 2975, 2928, 2896, 1637, 1381, 1273, 1090, 1050, 881, and 696 cm^{-1}. The shift of the broad O–H band from 3414 to 3400 cm^{-1} suggests that the

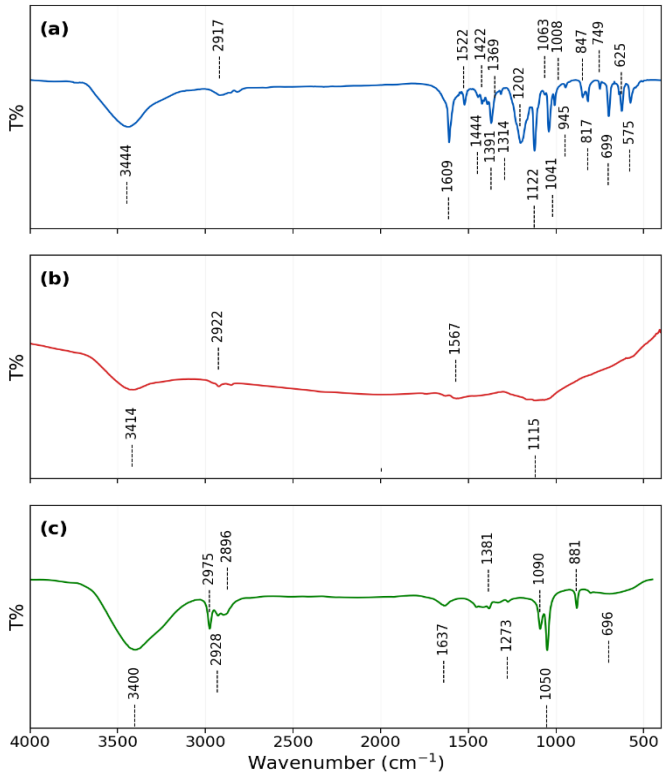


Figure 12. FTIR spectra of (a) MO, (b) pristine HSCA, and (c) MO-loaded HSCA after adsorption

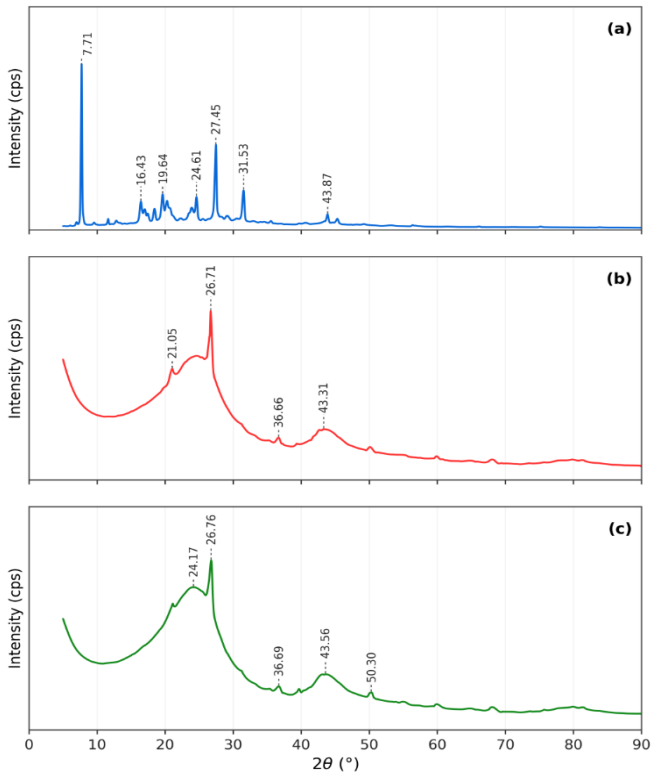


Figure 12. XRD patterns of (a) pristine MO, (b) pristine HSCA, and (c) MO-loaded HSCA after adsorption

hydrogen-bonding environment of HSCA surface hydroxyl groups was altered after adsorption. The appearance and/or intensification of C–H bands in the 2975–2896 cm^{-1} region supports the presence of adsorbed MO molecules on the HSCA surface. In addition, the band at 1637 cm^{-1} may arise from the overlap of aromatic C=C vibrations of HSCA and coupled azo–aromatic skeletal vibrations of MO. The bands observed at 1381 and 1273 cm-1 may be attributed to overlapping C–N, CH_3 deformation, and sulfonate-related vibrational contributions, while the bands at 1090 and 1050 cm^{-1} may be attributed to overlapping contributions from C–O vibrations of oxygen-containing groups on HSCA and S–O vibrations associated with MO [12,55,67].

Overall, the appearance of MO-related bands and the spectral changes observed after adsorption provide supporting evidence for the adsorption of MO onto HSCA. The observed changes in the O–H and aromatic skeletal regions, together with the overlapping C–N, C–O and sulfonate-related contributions, suggest changes in the local chemical environment of the HSCA surface upon MO adsorption. However, these FTIR observations are considered supportive rather than direct evidence of the specific adsorption mechanism.

To further evaluate the structural characteristics of HSCA and possible changes associated with MO adsorption, the XRD patterns of pristine MO, pristine HSCA, and MO-loaded HSCA are presented in Fig. 12. As shown in Fig. 12a, pristine MO exhibited a pronounced crystalline character, as evidenced by numerous sharp and intense diffraction peaks, particularly in the low- and intermediate-2θ regions. The highly intense reflection observed at approximately 8°, together with the subsequent sharp reflections, indicates the polycrystalline nature of MO, consistent with the XRD characteristics reported by Farag et al. (2011) [71].

In contrast, pristine HSCA (Fig. 12b) exhibited a broad diffraction halo, indicative of its predominantly disordered/amorphous structure. Similar broad diffraction features have been reported for hazelnut-shell-derived materials [72,73].

Following MO adsorption, the overall diffraction profile of MO-loaded HSCA (Fig. 12c) remained largely preserved, with no substantial alteration in its characteristic broad structural features. A similar preservation of the main diffraction features after MO adsorption was reported by Moussout et al. (2024) for raw walnut shell [74]. Notably, the characteristic sharp reflections of crystalline MO were not distinctly observed in the MO-loaded HSCA sample, suggesting that adsorption occurred without the formation of a distinct crystalline MO phase detectable by XRD.

The surface morphology of HSCA before and after MO adsorption was further examined by SEM, while EDX analysis was used to obtain complementary information on elemental composition (Fig. 13). Pristine HSCA exhibited a heterogeneous and irregular surface morphology characterized by rough regions and visible cavities or pore-like features. Similar heterogeneous and porous surface characteristics have been reported for hazelnut-shell-derived activated carbon [75]. Following MO adsorption, the overall heterogeneous morphology

was retained, although local differences in surface

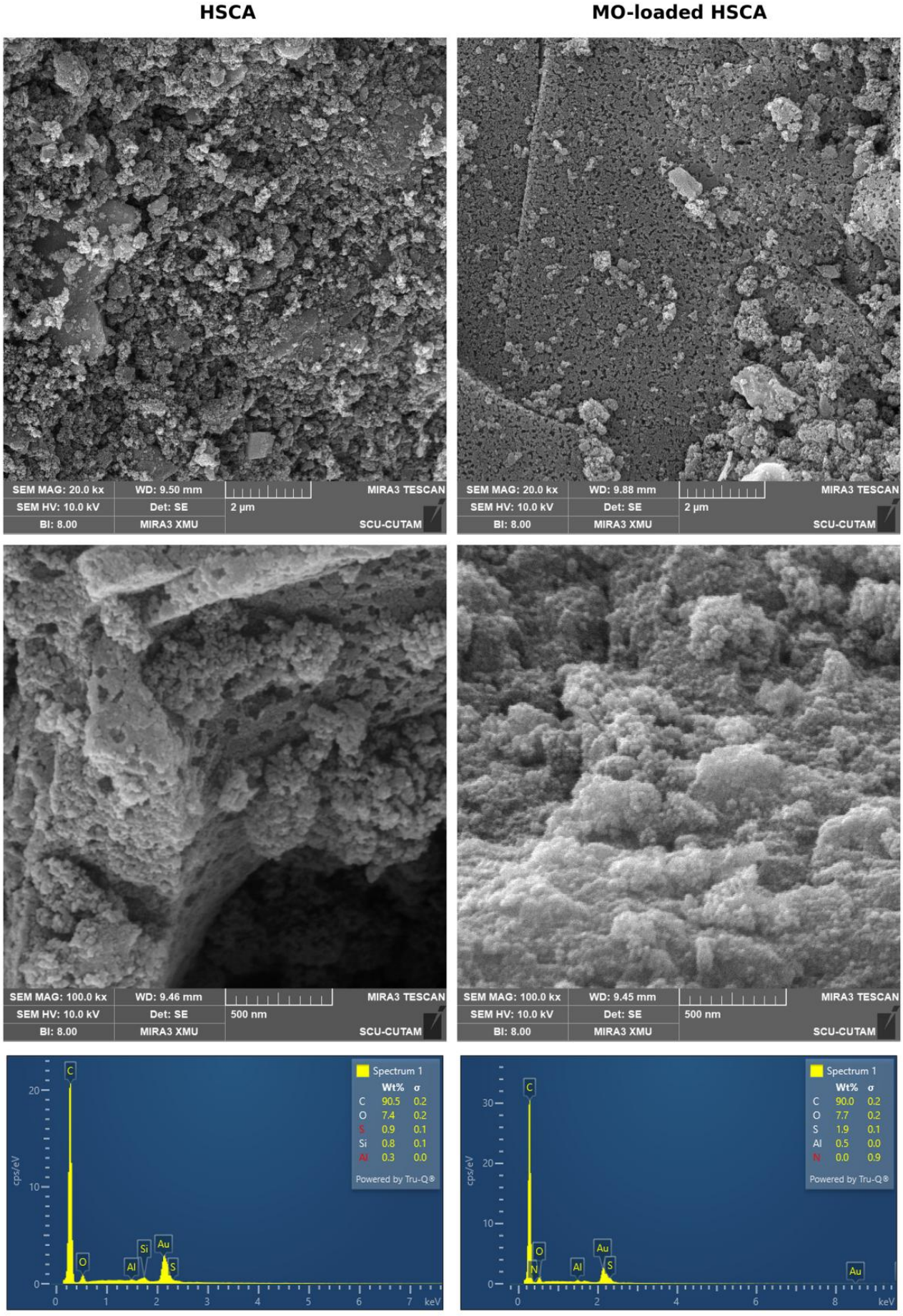


Figure 13. SEM images and EDX spectra of pristine HSCA and MO-loaded HSCA. EDX analysis of pristine HSCA showed a composition dominated by carbon and oxygen, consistent with the carbonaceous nature of the adsorbent and its appreciable oxygen content.

texture and the distribution of agglomerated regions were observed. The heterogeneous and irregular morphology observed by SEM provides morphological support for the non-uniform adsorption behavior suggested by the Freundlich analysis in Section 3.2. However, SEM alone does not establish energetic surface heterogeneity.

Minor contributions from S, Si, and Al were also detected in the analyzed pristine HSCA region. The local sulfur contribution increased from 0.9 wt% in pristine HSCA to 1.9 wt% in the analyzed MO-loaded HSCA region. Since sulfur is present in the sulfonate group of MO, the higher sulfur contribution after adsorption is consistent with the presence of MO on the analyzed HSCA surface region. Given the localized nature of EDX analysis and the elemental heterogeneity of the biomass-derived adsorbent, this observation is regarded as complementary rather than quantitative evidence of MO adsorption.

Taken together, the N_2 adsorption–desorption, FTIR, XRD, and SEM/EDX results provide complementary evidence for the physicochemical changes associated with MO adsorption onto HSCA. The N_2 adsorption–desorption results demonstrate a substantial loss of accessible surface area and pore volume, particularly within the microporous domains, consistent with partial pore filling and pore-mouth blocking. FTIR indicates changes in the local chemical environment of surface functional groups, while XRD shows that the overall disordered carbonaceous structure of HSCA is largely preserved after adsorption. The morphological changes observed by SEM and the increased sulfur contribution detected by EDX further support the presence of MO on the adsorbent surface. These characterization results are consistent with the experimentally observed adsorption behavior and provide complementary support for the surface charge and DFT results discussed in Section 3.4. However, the individual characterization techniques are not considered direct evidence of a specific adsorption mechanism. Rather, the combined experimental and computational findings suggest a cooperative adsorption scenario involving electrostatic attraction, pore accessibility and partial pore filling, and multiple non-covalent MO–surface interactions. The favorable adsorption behavior of HSCA can therefore be associated with the coexistence of an accessible micro–mesoporous pore network, oxygen-containing surface functionalities, and an aromatic carbon framework, which together provide both accessible adsorption domains and chemically diverse sites for MO–surface interactions.

4. Conclusion

This study provided an integrated evaluation of MO adsorption onto HSCA by combining kinetic and equilibrium modeling, diffusion analysis, apparent thermodynamic assessment, physicochemical characterization, surface-charge analysis, and DFT calculations. The nonlinear PFO model provided the most suitable empirical description of the kinetic data, whereas the Weber–Morris and Boyd analyses indicated that MO uptake could not be assigned to a single rate-controlling step and was instead consistent with contributions from external mass transfer and intraparticle diffusion. Comparative equilibrium modeling showed that Freundlich and Redlich–Peterson provided substantially better descriptions than Langmuir, consistent with non-ideal and heterogeneous adsorption behavior within the investigated concentration and temperature ranges. The apparent thermodynamic analysis indicated favorable and endothermic adsorption tendencies under the studied conditions. In addition, the reduction in BET surface area and accessible pore volume after adsorption was consistent with partial occupation or reduced accessibility of pore domains by MO.

The combined experimental and molecular-level findings support a cooperative adsorption process involving pore accessibility, surface heterogeneity, and multiple non-covalent interactions. Surface-charge analysis indicated favorable electrostatic conditions at pH 3.0, while FTIR, XRD, and SEM/EDX provided complementary evidence for MO uptake without indicating major structural disruption of the carbonaceous framework. DFT calculations further supported MO–HSCA interactions involving π-related interactions, dispersion contributions, and localized hydrogen-bonding or dipolar contacts. These findings should be interpreted as complementary evidence rather than as direct proof of a unique adsorption mechanism. Overall, the results support the potential of HSCA as a biomass-derived carbonaceous adsorbent for MO removal and demonstrate the value of combining equilibrium modeling, physicochemical characterization, and molecular-level calculations for interpreting adsorption behavior.

Ethical statement

This study did not involve human participants, animals, or clinical data. Therefore, ethical approval was not required.

Conflict of interest

The authors declare no conflict of interest.

Funding
This study received no financial support.

Author contributions
Nagihan Soyer: Conceptualization, supervision, methodology, validation, investigation, data curation, writing – original draft.

Sema Salgın: Methodology, validation, visualization, data curation, writing – review and editing.

Uğur Salgın: Software, validation, visualization, data curation, writing – review and editing.

Acknowledgments
The numerical calculations reported in this paper were partially performed at TUBİTAK ULAKBİM, High Performance and Grid Computing Center using TRUBA resources.

Use of generative AI
The authors used ChatGPT solely for English language editing, grammar refinement, and assistance in preparing the schematic workflow presented in Fig. 1. The tool was not used for data analysis, interpretation of results, or the generation of scientific conclusions. All final text, figure content, and scientific interpretations were reviewed, verified, and approved by the authors, who take full responsibility for the manuscript.

Data availability
All data analyzed during the study are included in this article.

References
[1] T. Robinson, G. McMullan, R. Marchant, P. Nigam, Remediation of dyes in textile effluent: A critical review on current treatment technologies with a proposed alternative, Bioresour Technol, 77, 2001, 247–255.
[2] G. Crini, Non-conventional low-cost adsorbents for dye removal: A review, Bioresour Technol, 97, 2006, 1061–1085.
[3] E. Forgacs, T. Cserháti, G. Oros, Removal of synthetic dyes from wastewaters: A review, Environ Int, 30, 2004, 953–971.
[4] A.A. Alghamdi, A.B. Al-Odayni, W.S. Saeed, A. Al-Kahtani, F.A. Alharthi, T. Aouak, Adsorption of Azo dye methyl orange from aqueous solutions using alkali-activated polypyrrole-based graphene oxide, Molecules, 24, 2019, 3685.
[5] N.S.M. Sayed, A.S.A. Ahmed, M.H. Abdallah, G.A. Gouda, ZnO@ activated carbon derived from wood sawdust as adsorbent for removal of methyl red and methyl orange from aqueous solutions, Sci Rep, 14, 2024, 5384.
[6] C. Diaz-Uribe, J. Ortiz, F. Duran, W. Vallejo, J. Fals, Methyl orange adsorption on biochar obtained from Prosopis juliflora waste: Thermodynamic and kinetic study, ChemEngineering, 7, 2023, 114.
[7] G. Crini, E. Lichtfouse, L.D. Wilson, N. Morin-Crini, Conventional and non-conventional adsorbents for wastewater treatment, Environ Chem Lett, 17, 2019, 195–213.
[8] X. Tan, Y. Liu, G. Zeng, X. Wang, X. Hu, Y. Gu, Z. Yang, Application of biochar for the removal of pollutants from aqueous solutions, Chemosphere, 125, 2015, 70–85.
[9] N.X. Loc, P.T.T. Tuyen, L.C. Mai, D.T.M. Phuong, Chitosan-modified biochar and unmodified biochar for methyl orange: Adsorption characteristics and mechanism exploration, Toxics, 10, 2022, 500.
[10] Z. Alasmary, M.A. Akanji, Iron-modified biochar derived from poultry manure for efficient removal of methyl orange dye from aqueous solution, Sustainability, 17, 2025, 6008.
[11] Z. Tigrine, O. Benhabiles, L. Merabti, N. Chekir, M. Mellal, S. Aoudj, Sustainable activated carbon from agricultural waste: A study on adsorption efficiency for humic acid and methyl orange dyes, Sustainability, 16, 2024, 9308.
[12] A.B. Al-Odayni, F.S. Alsubaie, N.A.Y. Abdu, H.M. Al-Kahtani, W.S. Saeed, Adsorption kinetics of methyl orange from model polluted water onto N-doped activated carbons prepared from N-containing polymers, Polymers, 15, 2023, 1983.
[13] İ.M. Hasdemir, E. Yılmazoğlu, S. Güngör, B. Hasdemir, Adsorption of acetic acid onto activated carbons produced from hazelnut shell, orange peel, and melon seeds, Appl Water Sci, 12, 2022, 271.
[14] N. Soyer, S. Salgın, U. Salgın, Data-driven predictive modeling and optimization of methyl orange adsorption onto hazelnut shell-derived activated carbon using RSM and ANN (abstract), 7th International Eurasian Conference on Science, Engineering and Technology, Jun 24-26, Ankara, 2026, Türkiye, 519–528.
[15] V.N. Klushin, W.M. So, V.M. Mukhin, T.A. Si, A.V. Nistratov, Method of producing crushed active coal, 2017, RU2605967C1.
[16] D. Özdeş, C. Duran, B. Şeker, V.N. Bulut, Removal of Pb(II) ions from aqueous solutions by Brevibacillus agri-loaded clay: Kinetic, isotherm, and artificial neural network modeling, Turk J Anal Chem, 8, 2026, 103–116.
[17] B. Kabak, Magnetic biochar derived from olive pomace for efficient tetracycline removal from water, Turk J Anal Chem, 7, 2025, 268–281.
[18] S. Lagergren, Zur theorie der sogenannten adsorption gelöster stoffe, K Sven Vetenskapsakad Handl, 24, 1898, 1–39.
[19] Y.S. Ho, G. McKay, The kinetics of sorption of divalent metal ions onto sphagnum moss peat, Water Res, 34, 2000, 735–742.
[20] D.C. Montgomery, E.A. Peck, G.G. Vining, Introduction to Linear Regression Analysis (6th edition), 2021, USA, Wiley.
[21] W.J. Weber, J.C. Morris, Kinetics of adsorption on carbon from solution, J Sanit Eng Div, 89, 1963, 31–59.
[22] G.E. Boyd, A.W. Adamson, L.S. Myers, The exchange adsorption of ions from aqueous solutions by organic zeolites. II. Kinetics, J Am Chem Soc, 69, 1947, 2836–2848.
[23] D. Reichenberg, Properties of ion-exchange resins in relation to their structure. III. Kinetics of exchange, J Am Chem Soc, 75, 1953, 589–597.
[24] I. Langmuir, The constitution and fundamental properties of solids and liquids. Part I. Solids, J Am Chem Soc, 38, 1916, 2221–2295.
[25] H. Freundlich, Über die adsorption in lösungen, Z Phys Chem, 57U, 1907, 385–470. https://doi.org/10.1515/zpch-1907-5723
[26] O. Redlich, D.L. Peterson, A useful adsorption isotherm, J Phys Chem, 63, 1959, 1024–1024. https://doi.org/10.1021/j150576a611
[27] Ü.C. Erim, Congo red removal from aqueous solution using 2-mercaptopropionic acid functionalized Fe_3O_4 magnetic nanoparticles, Turk J Anal Chem, 7, 2025, 361–369.
[28] H. Akaike, A new look at the statistical model identification, IEEE Trans Autom Control, 19, 1974, 716–723.
[29] G. Schwarz, Estimating the dimension of a model, Ann Stat, 6, 1978, 461–464.
[30] S.S. Shapiro, M.B. Wilk, An analysis of variance test for normality (complete samples), Biometrika, 52, 1965, 591–611.
[31] A. Wald, J. Wolfowitz, On a test whether two samples are from the same population, Ann Math Stat, 11, 1940, 147–162.
[32] U. Salgın, N. Soyer, S. Salgın, Y.E. Salgın, Integrated experimental, computational, and density functional theory analysis of m-nitrophenol adsorption and supercritical CO_2-assisted

regeneration on β-cyclodextrin nanosponges, Sep Purif Technol, 401, 2026, 138516.
[33] U. Salgın, İ. Alomari, N. Soyer, S. Salgın, Adsorption of Bisphenol A onto β-cyclodextrin–based nanosponges and innovative supercritical green regeneration of the sustainable adsorbent, Polymers, 17, 2025, 856.
[34] M.J. Frisch, G.W. Trucks, H.B. Schlegel, G.E. Scuseria, M.A. Robb, J.R. Cheeseman, Gaussian 16, 2016, Wallingford, CT: Gaussian, Inc.
[35] S. Salgın, U. Salgın, Y.E. Salgın, N. Soyer, pH-dependent complexation of ketoprofen with β-cyclodextrin and hydroxypropyl-β-cyclodextrin: Integrated experimental and computational insights, J Mol Struct, 1373, 2026, 146755.
[36] T. Lu, F. Chen, Multiwfn: A multifunctional wavefunction analyzer, J Comput Chem, 33, 2012, 580–592.
[37] T. Lu, A comprehensive electron wavefunction analysis toolbox for chemists, Multiwfn, J Chem Phys, 161, 2024, 082503.
[38] W. Humphrey, A. Dalke, K. Schulten, VMD: Visual molecular dynamics, J Mol Graph, 14, 1996, 33–38.
[39] K. Kuśmierek, A. Świątkowski, The influence of different agitation techniques on the adsorption kinetics of 4-chlorophenol on granular activated carbon, React Kinet Mech Catal, 116, 2015, 261–271.
[40] M.M. Nassar, Energy consumption and mass transfer during adsorption using gas and mechanical stirring systems, Water Res, 32, 1998, 3071–3079.
[41] J.P. Simonin, On the comparison of pseudo-first order and pseudo-second order rate laws in the modeling of adsorption kinetics, Chem Eng J, 300, 2016, 254–263.
[42] H.N. Tran, S.J. You, A. Hosseini-Bandegharaei, H.P. Chao, Mistakes and inconsistencies regarding adsorption of contaminants from aqueous solutions: A critical review, Water Res, 120, 2017, 88–116.
[43] K.Y. Foo, B.H. Hameed, Insights into the modeling of adsorption isotherm systems, Chem Eng J, 156, 2010, 2–10.
[44] N. Ayawei, A.N. Ebelegi, D. Wankasi, Modelling and interpretation of adsorption isotherms, J Chem, 2017, 3039817.
[45] B. Subramanyam, A. Das, Linearised and non-linearised isotherm models optimization analysis by error functions and statistical means, J Environ Health Sci Eng, 12, 2014, 92.
[46] N. Mohammadi, H. Khani, V.K. Gupta, E. Amereh, S. Agarwal, Adsorption process of methyl orange dye onto mesoporous carbon material–kinetic and thermodynamic studies, J Colloid Interface Sci, 362, 2011, 457–462.
[47] F. Liu, Z. Guo, H. Ling, Z. Huang, D. Tang, Effect of pore structure on the adsorption of aqueous dyes to ordered mesoporous carbons, Microporous Mesoporous Mater, 227, 2016, 104–111.
[48] Y. Liu, Is the free energy change of adsorption correctly calculated?, J Chem Eng Data, 54, 2009, 1981–1985.
[49] E.C. Lima, A. Hosseini-Bandegharaei, J.C. Moreno-Piraján, I. Anastopoulos, A critical review of the estimation of the thermodynamic parameters on adsorption equilibria. Wrong use of equilibrium constant in the Van't Hoof equation for calculation of thermodynamic parameters of adsorption, J Mol Liq, 273, 2019, 425–434.
[50] H.N. Tran, E.C. Lima, R.S. Juang, J.C. Bollinger, H.P. Chao, Thermodynamic parameters of liquid–phase adsorption process calculated from different equilibrium constants related to adsorption isotherms: A comparison study, J Environ Chem Eng, 9, 2021, 106674.
[51] J.T. Bullerjahn, S.M. Hanson, Extracting thermodynamic properties from van 't Hoff plots with emphasis on temperature-sensing ion channels, Temperature, 11, 2024, 60–71.
[52] M. Kosmulski, The pH-dependent surface charging and points of zero charge, J Colloid Interface Sci, 353, 2011, 1–15.
[53] J. Gutierrez-Martinez, V. Hernandez-Montoya, M.A. Montes-Moran, M. Perez-Mendoza, Point of zero charge, isoelectric point, and potential of zero charge on activated carbons: A comprehensive interpretation about their interrelation, Curr Opin Solid State Mater Sci, 40, 2026, 101247.
[54] M. Kosmulski, pH-dependent surface charging and points of zero charge. IV. Update and new approach, J Colloid Interface Sci, 337, 2009, 439–448.
[55] C. Moreno-Castilla, Adsorption of organic molecules from aqueous solutions on carbon materials, Carbon, 42, 2004, 83–94.
[56] S. Grimme, Do special noncovalent π–π stacking interactions really exist?, Angew Chem Int Ed, 47, 2008, 3430–3434.
[57] S. Grimme, J. Antony, S. Ehrlich, H. Krieg, A consistent and accurate ab initio parametrization of density functional dispersion correction (DFT-D) for the 94 elements H-Pu, J Chem Phys, 132, 2010, 154104.
[58] S.F. Boys, F. Bernardi, The calculation of small molecular interactions by the differences of separate total energies. Some procedures with reduced errors, Mol Phys, 19, 1970, 553–566.
[59] D.L. Carballeira, N. Ramos-Berdullas, I. Pérez-Juste, J.L.C. Fajín, M.N.D.S. Cordeiro, M. Mandado, A computational study of the interaction of graphene structures with biomolecular units, Phys Chem Chem Phys, 18, 2016, 15312–15321.
[60] A. Molla, Y. Li, B. Mandal, S.G. Kang, S.H. Hur, J.S. Chung, Selective adsorption of organic dyes on graphene oxide: Theoretical and experimental analysis, Appl Surf Sci, 464, 2019, 170–177.
[61] X. Cheng, H. Deng, Z. Liu, C. Ding, X. Liang, H. Rong, Multi-stage adsorption of methyl orange on the nitrogen-rich biomass-derived carbon adsorbent: DFT and MD evaluation, Chemosphere, 338, 2023, 139218.
[62] P. Politzer, J.S. Murray, The fundamental nature and role of the electrostatic potential in atoms and molecules, Theor Chem Acc, 108, 2002, 134–142.
[63] A.E. Reed, L.A. Curtiss, F. Weinhold, Intermolecular interactions from a natural bond orbital, donor-acceptor viewpoint, Chem Rev, 88, 1988, 899–926.
[64] E.R. Johnson, S. Keinan, P. Mori-Sánchez, J. Contreras-García, A.J. Cohen, W. Yang, Revealing noncovalent interactions, J Am Chem Soc, 132, 2010, 6498–6506.
[65] M. Thommes, K. Kaneko, A.V. Neimark, J.P. Olivier, F. Rodriguez-Reinoso, J. Rouquerol, K.S.W. Sing, Physisorption of gases, with special reference to the evaluation of surface area and pore size distribution (IUPAC Technical Report), Pure Appl Chem, 87, 2015, 1051–1069.
[66] K.A. Cychosz, M. Thommes, Progress in the physisorption characterization of nanoporous gas storage materials, Engineering, 4, 2018, 559–566.
[67] B. Grégoire, J.L. Bantignies, R. Le Parc, B. Prelot, J. Zajac, G. Layrac, D. Tichit, G. Martin-Gassin, Multiscale mechanistic study of the adsorption of methyl orange on the external surface of layered double hydroxide, J Phys Chem C, 123, 2019, 22212–22220.
[68] L. Wu, J. Ding, Y. Zheng, W. An, S. Deng, Study on the adsorption properties of methyl orange by natural one-dimensional nano-mineral materials with different structures, Sci Rep, 11, 2021, 10640.
[69] H.P. Boehm, Surface oxides on carbon and their analysis: A critical assessment, Carbon, 40, 2002, 145–149.
[70] L. Zhang, X. Ding, H. Rong, Z. Chen, Coconut-based activated carbon fibers for efficient adsorption of various organic dyes, RSC Adv, 8, 2018, 42280–42291.
[71] A.A.M. Farag, A.M. Mansour, A.H. Ammar, M.A. Rafea, Characterization of electrical and optical absorption of organic based methyl orange for photovoltaic application, Synth Met, 161, 2011, 2135–2143.
[72] N. Agilee, E. Yılmazoğlu, İ.M. Hasdemir, S. Güngör, B. Hasdemir, Hazelnut shells as a tenable biosorbent for basic red 18 azo dye removal, Separations, 11, 2024, 343.
[73] T.J. Al-Musawi, G. McKay, A. Kadhim, M.M. Joybari, D. Balarak, Activated carbon prepared from hazelnut shell waste and

magnetized by Fe3O4 nanoparticles for highly efficient adsorption of fluoride, Biomass Convers Biorefin, 14, 2024, 4687–4702.
[74] H. Moussout, H. Ahlafi, M. Aazza, H. Boualy, Towards a profound understanding of methyl orange removal from industrial wastewater using a raw walnut shell: Kinetics, equilibrium, thermodynamics, and statistical physics calculations, J Mol Liq, 410, 2024, 125606.
[75] E. Demirbas, N. Dizge, M.T. Sulak, M. Kobya, Adsorption kinetics and equilibrium of copper from aqueous solutions using hazelnut shell activated carbon, Chem Eng J, 148, 2009, 480–487.